# Chapter 1

# Introduction

Flux pinning of both high and low temperature superconductors has recently attracted great interest because of their relevance to applications as well as the fundamental viewpoints. In the mixed state of the type II superconductor, magnetic fields can penetrate into the superconductor inhomogeneously in the form of Abrikosov vortices which tend to arrange themselves in a triangular vortex lattice [1]. Each vortex has a magnetic field of flux quantum and is surrounded by circulating supercurrents. The vortices can be perturbed by the defects that pin the vortex. Thus, the vortex-vortex and vortex-pin interactions in the superconductor give rise to a rich variety of static and dynamical phases [2]. The dynamic properties of the vortices show many interesting behaviors in the superconductor. These behaviors include avalanches, stick-slip dynamics [3], thresholds [4], and rectification for motion [5], nonlinear and hysteretic dynamic response and plastic/elastic motion [6].

One important method to study the dynamic properties of the vortices is injected current in superconductors, because energy dissipation occurs during the vortex motion. Many technological applications of the superconducting materials are determined by their ability to support high current densities with minimal energy

dissipation. The flux pinning effect is a fundamental characteristic for the superconductors with defects. The onset of the energy dissipation is related to the critical current of the materials. Thus, we can determine the critical current to understand the pinning properties of the superconductor. It is necessary to enhance the vortex pinning by arranging the pinning centers such that they can match the vortex lattice at a given magnetic field. Pinning effects were first demonstrated by Daldini et al. for periodic thickness modulation of superconducting films [7]. They gave evidence for matching of the two-dimensional vortex lattice with the one-dimensional periodic pinning structure. Following this initial work, Fiory et al. also demonstrated matching effects for triangular pinning arrays of holes in an Al superconducting film [8]. Recently it has been demonstrated that the matching effects for the hole array can be used to reduce low frequency noise in rf-SQUIDS [9].

New tools for lithography on a small scale allow access to the dimensions which are comparable to the relevant length scales in a superconductor. Nanolithography based on electron-beam direct writing has been used to prepare submicrometric structures with specified geometries [10-12]. Different shapes of pinning centers and arrays, and different materials have been explored from the experimental results [13-16, 21, 25] as well as the theoretical simulations [17-20, 22, 26]. As it has been shown, the dc magnetoresistance of superconducting thin films

with periodic arrays of pinning centers shows minima when the vortex lattice matches the unit cell of the array. These minima are sharp and equal spacing separated by the same magnetic field. The number of vortices (n) per array unit cell can be known by the minima of the magnetoresistance, in which the first minimum corresponds to one vortex per unit cell, the second minimum to two vortices per unit cell, and so on.

Moreover, the superconducting coherence length governs the maximum number of vortices that could be pinned in each one of the pinning center. Herein, one important aspect for the pinning mechanism is that the artificial pinning center is occupied by either one vortex or multivortex. Therefore, for selected values of the applied magnetic field, the number of pinned vortices and interstitial vortices are worth to find out. For small pinning sites, only a single vortex will be trapped at an individual pinning center and the additional vortices locate at the interstitial position. This has been imaged using Lorentz microscopy by Harada et al. [21]. The vortex positions observed in these experiments were then well reproduced by numerical simulations by Reichhardt, and Nori [22]. Another possibility at the matching fields is that multiple vortices can occupy individual pinning sites. For an isolated pinning center the saturation number of vortices is $n_s = \frac{d}{2\xi}$ (the maximum possible number of the vortices trapped by the single insulating), where d is the diameter of a defect and $\xi$ is the superconducting coherence [23]. Bitter decoration technique was used

by Bezryadin et al. to investigate multivortex states [24]. That work demonstrates that the size of the pinning sites can influence the number of the vortices trapped at a single site. Furthermore, Hoffmann et al. have experimentally studied the number of vortices per array unit cell and per pinning site, taking into account the dots size and the unit cell parameters [25]. Numerical simulations of scaling of the critical current for varied pinning strength are studied and fully supported this idea [26]. Recently, Peeter also studies different vortex configurations in a superconducting film with a square array of antidots within the Ginzburg-Landau theory [20].

The early interests and explorations were mainly focused on symmetry potential of pinning effect for the vortices. Brandt first used asymmetric shape of pinning traps on superconductor [27]. Several schemes were proposed to control vortex motion and have attracted attentions to study ratchet effects in superconductor [28, 29]. Extension of this idea was made by Wambauch et. al, who supposed that the vortex pinning energy is infinite except in specially designed saw-tooth shape channels with 2D profile [30]. They have made interesting proposals to create vortex diodes or vortex lenses, that is, concentration or dispersion the vortices in special parts of the sample. Beside the topics of fluxon optic [30], the ratchet-like pinning potential is useful for applications in superconducting samples, including the removal of flux trapped in superconducting devices [31, 32], and logic devices [33], etc. Arira

Tonomura gave an interesting metaphor for controlling the vortex motion [34]. A stunt was used in his metaphor, that is, we rapidly pull a tablecloth from underneath the dinner plates on top of it. It is well known that if we pull fast enough, and the plates do not move. Pull slowly, and the dishes move together with the tablecloth. Then we fast pull the tablecloth to the right followed by a slow motion back to the left. The result is a movement of the plates to the left. The same principles can be applied for controlling the motion of flux quanta. The alternating drive current to the vortices, is like the movement of the tablecloth to the plates. This gave us another approach to study the motion of vortices.

From the experimental point of view, some progress has been reported related to superconducting circuits, and very recently vortex motion ratchet effect has been reported in superconducting films with artificially fabricated arrays of asymmetric pinning centers [35, 36]. They show that superconducting Pb and Nb films with asymmetric periodic pinning centers, subject to a magnetic field perpendicular to the film plane, exhibit tunable AC current rectification. AC currents are applied in the superconducting thin film and the net vortex flow under ac drive will give rise to dc responds (i.e. generate a uniform DC electric field along the direction of the AC current). Another way to create a net vortex flow with an AC current drive is by using a gradient of the vortex pinning potential. Similar results have been obtained for

quasi-regular array of symmetric pinning centers in our research. A spacing-graded array of submicrometer-scaled holes on the niobium thin films was studied by our group. The key ingredient of this idea is the long-range interaction between vortices. The appearance of the vortex rectification can be caused by long-range interaction between vortices which change the threshold of pinning energy at every pinning site.

This dissertation is devoted to the study of the vortex rectification in spacing-graded array of defects and is mainly classified into two subjects. The first subject is concerned with pinning effect in regular array while the second one presents the characteristics of vortex motion in irregular array. Overall, the dissertation is divided into 5 chapters.

This thesis is organized as follows. Chapter 2 gives a brief introduction of theoretical background on vortex physics in superconductors. We will introduce the typical process steps of numerical simulation. Next, the experimental details are presented in Chapter3. The standard EB lithography incorporating RIE etching technique to fabricate the nanometer array of holes on the substrate is demonstrated. The experimental results for a variety of samples are shown in Chapter 4. From chapter 4-1 to chapter 4-2, we get into the first subject concerning with the pinning properties of regular array. Then we will give a conclusion by comparing the characteristic from many published papers. In addition, we will review the pinning

mechanisms with particular emphasis from several published papers. The main subject starts from Chapter 4-3. Two different gradients of the samples have been studied in this thesis and these results are discussed in detail in Chapter 4-4. A brief conclusion is finally given in Chapter 5.

# Chapter 2

# Basic Theory

---

In this chapter some basic theoretical ideas about vortices in superconductors are briefly introduced. First we will discuss the basic properties of type II superconductors (see Section 2.1) and following that we will show some of the relevant vortex physics (see Section 2.2). Finally, we will show some ideas of the theoretical simulation for the vortex lattice in superconductor with regular array of defects (see Section 2.3).

## 2-1 Type II superconductors

Superconducting materials are divided into two types of superconductors depending on their characteristic behavior in the presence of a magnetic field. For $\kappa < 1/\sqrt{2}$, the superconducting material is called a type I superconductor. For $\kappa > 1/\sqrt{2}$, the superconducting material is called a type II superconductor(like for the Nb films used in our experiments) [1]. A schematic magnetic field-temperature phase diagram for type II superconductors is shown in Figure 2.1. At low temperatures and at magnetic fields below the lower critical field $H_{c1}$, the material is superconducting with an infinite conductivity (zero resistivity). This is the so called Meissner effect and it occurs in both type I and type II superconductors. The material is strongly diamagnetic so that the superconducting material expels any magnetic field form its interior. For high enough magnetic fields and/or temperatures the superconducting material is in its normal state with finite conductivity. For type II superconductors mixed state is in between the normal and the Meissner state at temperature below $T_c$.

The range of the mixed state is at intermediate magnetic fields between the lower ( $H_{c1}$ ) and higher( $H_{c2}$ ) critical field. The mixed state is characterized by the penetration of the magnetic field inside the material forming a lattice of vortices (see Figure 2.1). The magnetic field is concentrated along flux lines and each of these vortices has a quantized magnetic flux of $\Phi_0 = \frac{hc}{2e} = 20.7 G\mu m^2$.

For the characteristic behavior of $\kappa$ in superconductors there are two important length scales:

(i) the coherence length ($\xi$)

(ii) the magnetic penetration depth ( $\lambda$ ).

The coherence length gives the length scale over which the superconducting order parameter can vary, and as a result it also gives the length scale on which the density of superconducting electrons can change. On the other hand the magnetic penetration depth determines, on which length scale a magnetic field penetrates a superconductor. The ratio of these two length scales is called the Ginzburg-Landu parameter.

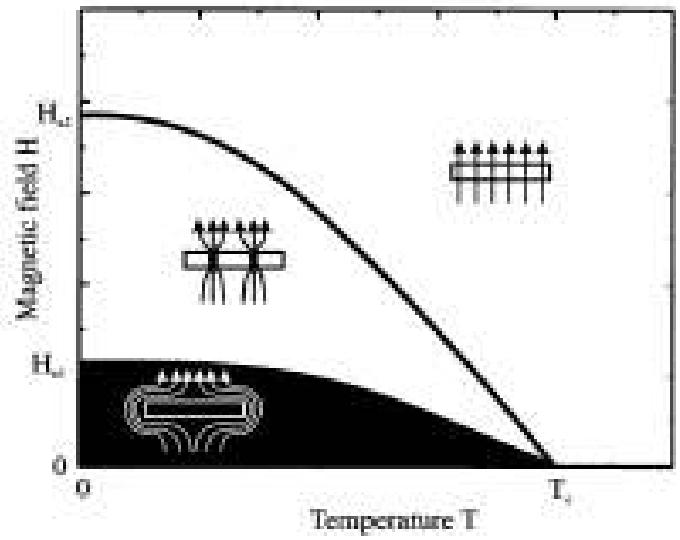

Since the screening currents in the superconductor circle around these magnetic flux lines, they are also referred to as superconducting vortices. The coherence length and the magnetic penetration depth in superconducting thin films can vary significantly from the published bulk values. The main reason for this is that these films have enough imperfections; such that they may have to be considered as being in the dirty limit. In this case the mean free path $l$ will limit these lengths in the following way:

$$\xi(0) = \sqrt{\xi_0 l}$$

$$\lambda(0) = \lambda_0 \sqrt{1 + \frac{\xi_0}{l}}$$

Here $\xi_0$ and $\lambda_0$ denote the clean limit values at zero temperature, while $\xi(0)$ and $\lambda(0)$ are the dirty limit values at zero temperature.

The transition from the mixed state to the normal state, at the upper critical field $H_{c2}$, occurs when the normal cores of the vortices overlap, such that there is no superconducting volume of the material left, and is given by

$$H_{c2} = \frac{\Phi_0}{2\pi\xi^2(T)}$$

Both $\xi$ and $\lambda$ are temperature dependent and diverge close to $T_c$. The tempterature dependence of the coherence length close to $T_c$ for the clean the dirty limit respectively is

$$\xi(T) = 0.74 \frac{\xi_0}{\sqrt{1 - \frac{T}{T_c}}} \text{ (clean)},$$

$$\xi(T) = 0.855 \frac{\sqrt{\xi_0 l}}{\sqrt{1 - \frac{T}{T_c}}} \text{ (dirty)}.$$

The temperature dependence of the magnetic penetration depth $\lambda$ close to $T_c$ is empirically given by

$$\lambda(T) = 0.74 \frac{\xi(T)}{\sqrt{1-\left(\frac{T}{T_c}\right)^4}}$$

which resembles closely the functional dependence expected from various theories. The thickness of the Nb thin films in our experiments are 100 nm, and thus comparable to the magnetic penetration depth. Since the screening currents, which are responsible for the finite penetration of the magnetic field, are restricted to the thickness $t$, this leads to a new effective magnetic penetration depth $\Lambda$ in the thin films:

$$\Lambda(T) = \frac{\lambda^2(T)}{t}$$

Notice that this gives rise to an even faster divergence of $\Lambda$ and $\lambda$ are also very important for describing the mixed state. The vortices in the mixed state have a normal-conducting core, whose radius $r$ equals the coherence length $\xi$. The magnetic penetration depth $\lambda$ on the other hand determines the distance over which individual vortices interact. Due to the repulsive interaction between the vortices, the vortices try to be separated from each other as far as possible. This is best accomplished by the vortices being arranged on a regular lattice, like a square or hexagonal lattice. The energetic difference between these two vortex configurations is very small and it favors a hexagonal arrangement. Indeed most experiments typically show a hexagonal vortex lattice, but structural anisotropies can also stabilize a distorted hexagonal, square, or rectangular lattice of the vortices. The relationship between the magnetic field and the distance a between the vortices for the square and hexagonal lattices as follows:

$$B = \frac{2\Phi_0}{\sqrt{3}a^2} \quad \text{(hexagonal)}$$

$$B = \frac{\Phi_0}{a^2} \quad \text{(square)}$$

## 2-2 Basic vortex physics

The presence of vortices in the superconductor has important consequences for some of the physical properties. In particular the transport and magnetization properties can give a lot of information about the vortices. If an electrical current is applied to a type II superconductor in the mixed state, then there is a Lorentz force

$$\vec{F} = \vec{j} \times \frac{\Phi_0 \vec{n}}{c}$$

acting on each vortex. Here $\vec{j}$ is the current density and $\vec{n}$ is the direction of the applied magnetic field. Therefore in absence of any other force the vortices tend to move perpendicular to the applied electrical current.

If the vortices move with a velocity $\vec{v}$, then they will essentially induce an electrical field

$$\vec{E} = \vec{B} \times \frac{\vec{v}}{c}$$

parallel to the applied current $\vec{j}$. If one assumes now a simple viscous drag force proportional to the velocity of the vortices

$$\vec{F} = -\eta \vec{v},$$

with a viscous drag coefficient $\eta$, then there is a simple expression for the flux flow Magnetoresistance in the mixed state. One gets:

$$\rho = \frac{E}{j} = B \frac{\Phi_0}{\eta c^2}$$

Thus in the mixed state the resistivity $\rho$ simply increases linearly with the magnetic field, as long as the drag coefficient $\eta$ is independent of the magnetic field.

A more careful analysis gives the result

$$\rho_f = \frac{B}{H_{c2}}\rho_n ,$$

with $\rho_f$ being the flux flow resistance and $\rho_n$ the normal state resistance.

Since the movement of the vortices will give rise to a non-zero resistivity in the mixed state, the superconductor will only have a zero resistance if the vortices are prevented from moving. This can be achieved by pinning the vortices into fixed positions. Pinning can result from any inhomogeneity of the superconducting material, such as impurities grain boundaries, etc. theses spatial inhomogeneities of the materials give rise to local variation of $\xi, \lambda$, and $H_{c2}$ and this causes in turn local variations of the free energy per unit length of a flux line. Thus some locations of the vortices are favored over others, which results in the pinning of the vortices. The depinning, and thus the onset of a non-zero resistance, will occur when the Lorentz force exceeds the pinning force $F_c$. Thus by simply equating the pinning force with the Lorentz force one obtains a simple expression for the critical current density (the minimum current necessary to have vortex motion in the mixed state):

$$j_c = c\frac{F_c}{\Phi_0} = c\frac{f_c}{B},$$

where $f_c$ is the pinning force density. Thus for a magnetic-field-independent pinning force the critical current will decrease as $1/B$.

As mentioned before, the vortices are normally arranged on a regular lattice. If the pinning centers are also distributed on a periodic array, the vortex lattice and the periodic pinning array. Since the vortex-vortex distance varies with applied field, the geometric matching will only occur at specific magnetic fields. In particular the first magnetic field at which geometric matching occurs corresponds to the vortex density and the pinning center density being equal. Thus this first matching field is:

$$H_1 = n\Phi_0 ,$$

where is the density of pinning centers. As will be seen later, geometric matching can also occur, when the vortex density is an integer multiple of the pinning center density. This defines the higher order matching fields

$$H_m = mH_1,$$

with m being an integer.

## 2-3 Simulation and Results

Numerical simulations allow exact control of microscopic parameters, such as pin strength and density, and provide both microscopic information, such as individual vortex motion, and macroscopic information, such as voltage signals.

For comparison of simulation and experiment, it is now possible to study much more realistic and complicated models using molecular-dynamics (MD) simulation. The simulation is an infinite slab with a magnetic field H=Hz applied parallel to the surface. In addition, it is considered that the system consist of rigid vortices and straight columnar pins. Thus this 3D slab can transform into 2D slice, which is more similar to what we studied in experiments.

For superconductors, the flux penetrates into a type-II superconductor in the form of discrete quantized vortices that repel each other and are attracted by defects in the superconducting material. As an external field is slowly increased, a gradient in the vortex density develops and drives vortices into the material. Then, additional flux lines enter the sample and occasionally cause large disturbances. A balancing pinning force holds the vortices in a meta-stable state. To model the MD simulation, we can add a vortex to the unpinned region. Vortex enters the superconducting slab under the force of their mutual repulsion and pass through a pinned region with periodic boundary conditions. The length scale of the system is set in a unit of penetration

depth. The superconducting system has a pinned region from $18\lambda \times 18\lambda$ to $72\lambda \times 72\lambda$

The vortex-vortex repulsive interaction is correctly represented by a modified Bessel function, $K_1\left(r/\lambda\right)$, cut off beyond $r = 6\lambda$ where the force is quite small. The vortices also interact with a large number of nonoverlapping short-range attractive parabolic potential wells of radius $\xi_p = 0.1\lambda - 0.3\lambda$, far less than vortex-vortex interaction cutoff of $6\lambda$.

In addition, all force studied in this simulation, such as the maximum pinning force and driving force in this study, is in units of $f_0 = \frac{\Phi_0^2}{8\pi^2\lambda^3}$. Magnetic field is in units of $\Phi_0/\lambda^2$, where $\Phi_0$ is the flux quantum. Inside the sample, the interacting vortices are driven by a Lorentz force over a quenched pinning background. Thus, the overdamped equation of motion can numerically be integrated as follow:

$$f_i = f_i^{vv} + f_i^{vp} + f_d + f_i^T = \eta v_i$$

Here, $f_i$ is the total force acting on vortex $i$, $f_i^{vv}$ is the force on $i$th vortex due to interaction force, $f_d$ is the driving force, and $f_i^T$ is the thermal force; $v_i$ is the net velocity of vortex i and $\eta$ is the viscosity, which is set equal to unity. The vortex-vortex interaction between two vortices located at $r_i$ and $r_j$ is correctly modeled by a modified Bessel function. Thus the force acting on a vortex $i$ due to other vortices is

$$f_i^{vv} = \sum_{j=1}^{N_v} f_0 K_1\left(\frac{|r_i - r_j|}{\lambda}\right)\hat{r}_{ij}$$

where $\hat{r}_{ij} = \frac{r_i - r_j}{|r_i - r_j|}$.

The pinning is modeled as $N_p$ short-range parabolic wells located at positions . The pinning force is

$$f_i^{vp} = \sum_{j=1}^{N_v} \left( \frac{f_p}{r_p} \right) \left| r_i - r_k^{(p)} \right| \Theta \left( \frac{r_p - \left| r_i - r_k^{(p)} \right|}{\lambda} \right) \hat{r}_{ik}^{(p)}$$

where $\Theta$ is the Heaviside step function, $f_p$ is the maximum pinning force, $N_p$ is the number of pinning sites, and $\hat{r}_{ij}^{(p)} = \dfrac{r_i - r_k^{(p)}}{\left| r_i - r_k^{(p)} \right|}$.

The driving force $f_d$ is modeled as a constant force that is slowly increased or decreased linearly with time.

The thermal force $f_i^T$ has the properties:

$$\left\langle f_i^T \right\rangle = 0$$

$$\left\langle f_i^T(t) f_j^T(t') \right\rangle = 2\eta k_B T \delta_{ij} \delta(t - t').$$

To find the vortex ground state, we can gradually cool a fixed number of randomly moving vortices form a high temperature to T=0. Figure 2-2 shows a series of vortex lattice orderings after annealing for square and triangle pinning array from the work of C. Reichhardt [22].

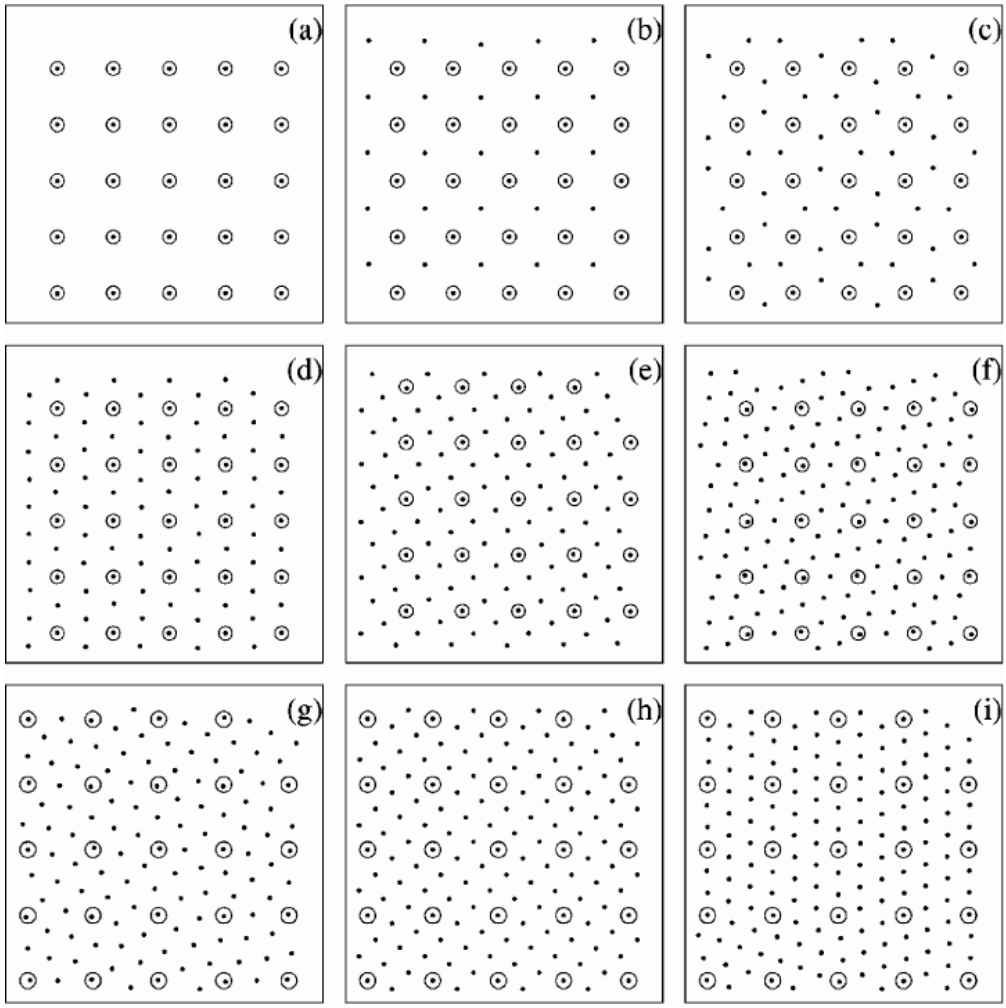


**Fig. 2-2 Numerical simulation of vortex positions at various matching fields for a square pinning array. Adapted from Ref. [22].**

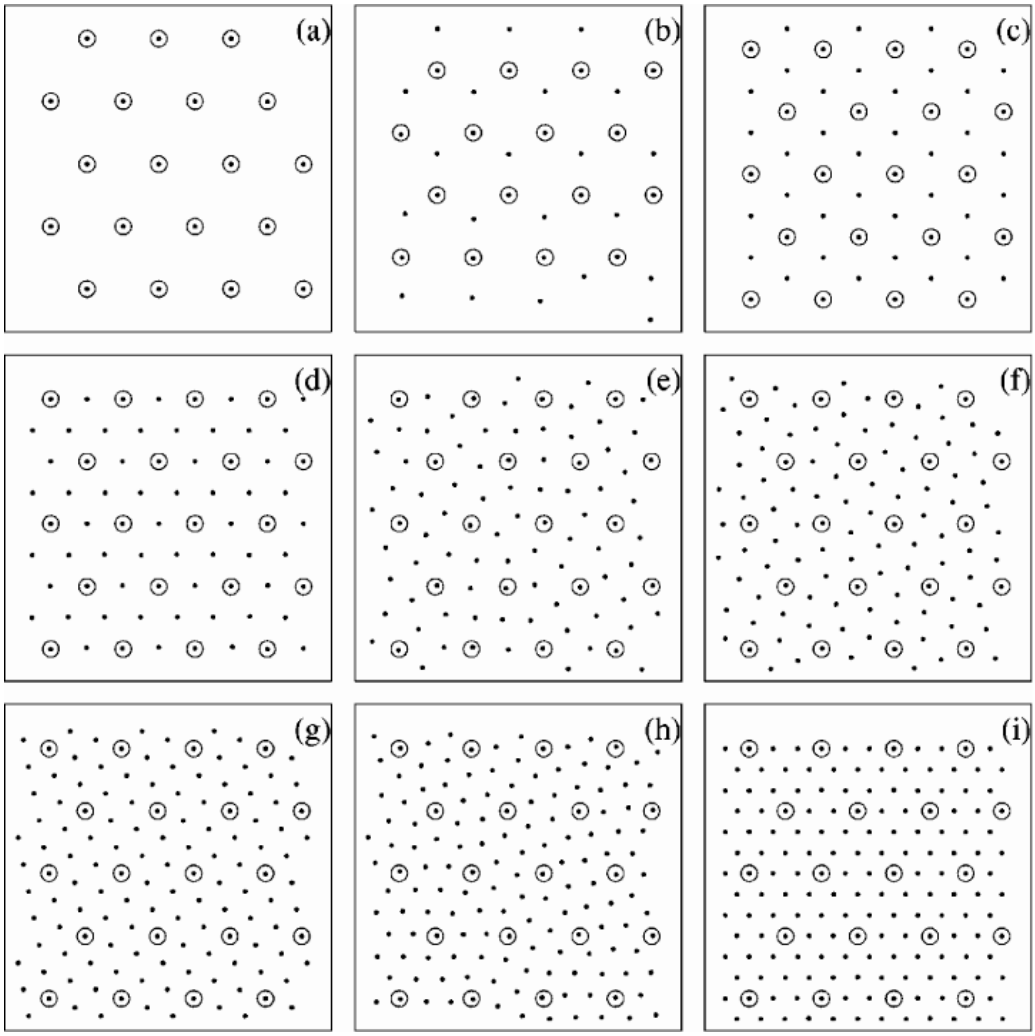


**Fig. 2-3 Numerical simulation of vortex positions at various matching fields for a triangular pinning array. Adapted from Ref. [22].**

# Chapter 3

## Fabrication process and measurement techniques

---

This chapter will describe the experimental details for measuring the vortex matching effects in Nb films. First the preparation of the samples and their characterization is explained (see Section 3.1). Following this, the transport measurements (see Section 3.2) are described and various criteria for defining several physical properties, such as the critical current or the magnetoresistance are presented.

## 3.1 Sample preparation

The fabrication procedure for a regular structure of submicro-holes which serve as flux pinning centers is shown in Fig. 3-1. The sample preparation is done in several steps. First, electron-beam lithography is used to define the periodic pinning arrays on polymethyl methacrylate (PMMA), as seen in Section 3-1-1. In general, the pattern is defined over a $10 \times 50 \mu m^2$. Second, a reactive ion etcher (RIE) was used to transfer the hole arrays into the $Si_3N_4$ film (see Section 3-1-2). Third, electron beam lithography was again used to open a four-probe shape trench in PMMA, in which care was taken to align the hole array sitting in the center part of the four-probe trench. Finally, a superconducting film is deposited on top of the patterned substrate (see Section 3-1-3).

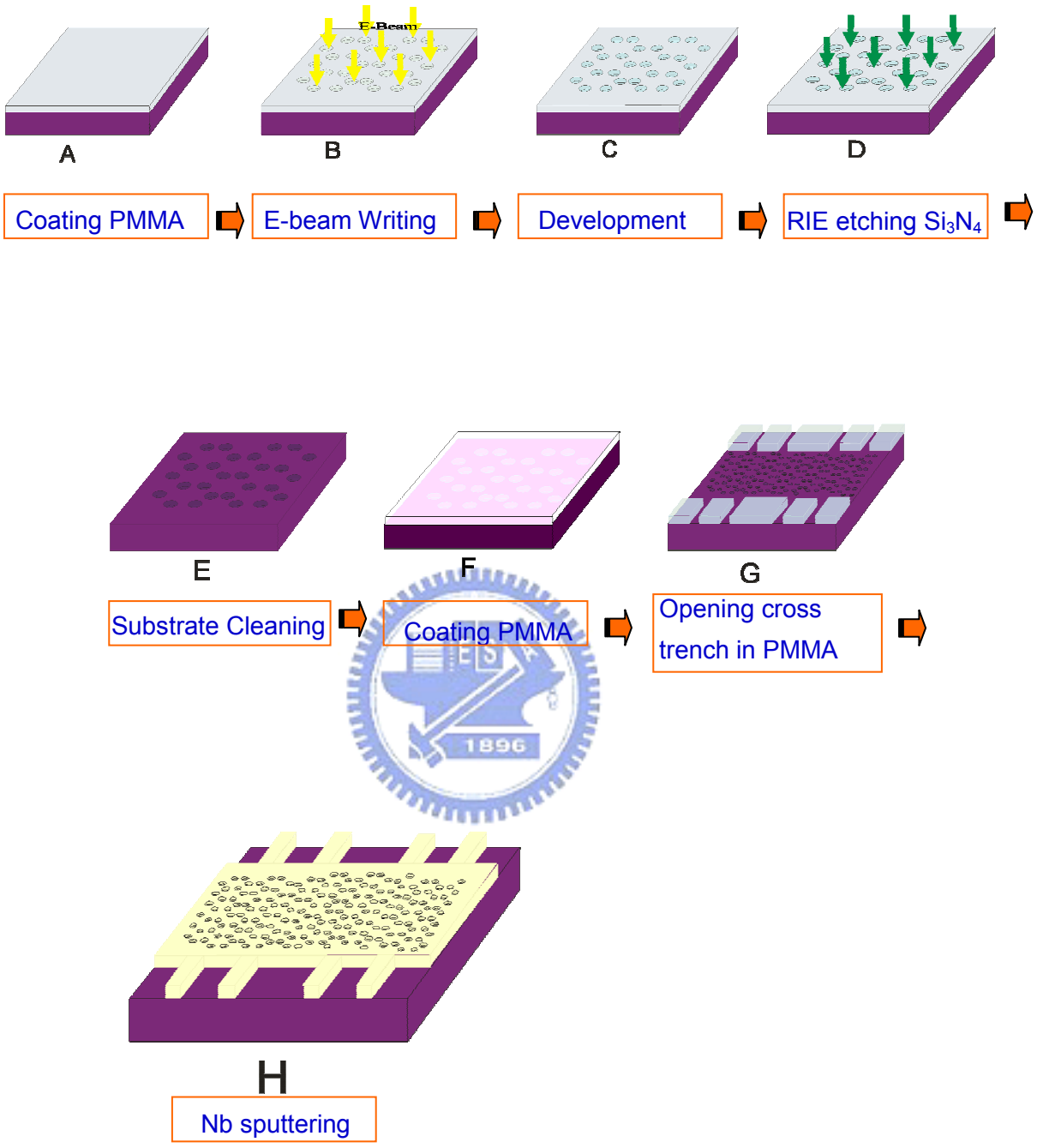


Fig. 3-1 Schematic of the electron-beam lithography and lift-off process.

### 3-1-1 E-beam lithography

The recent development of new lithographic techniques has been crucial for the advancement of research in these submicrometric structures. Due to the superiority of the shorter material wavelength of electrons (0.2-0.5 Å), electron beam (EB) lithography is widely used, where the desired pattern is defined by an electron beam of a scanning electron microscope (SEM). A conventional EB lithography system comprises a scanning EB across a substrate coated with a resist film, methyl methacrylate (PMMA), which is sensitive to electrons, followed directly defining nanometer patters in the resist film through computer-aided-design and beam breaking system without any photo mask design is advance.

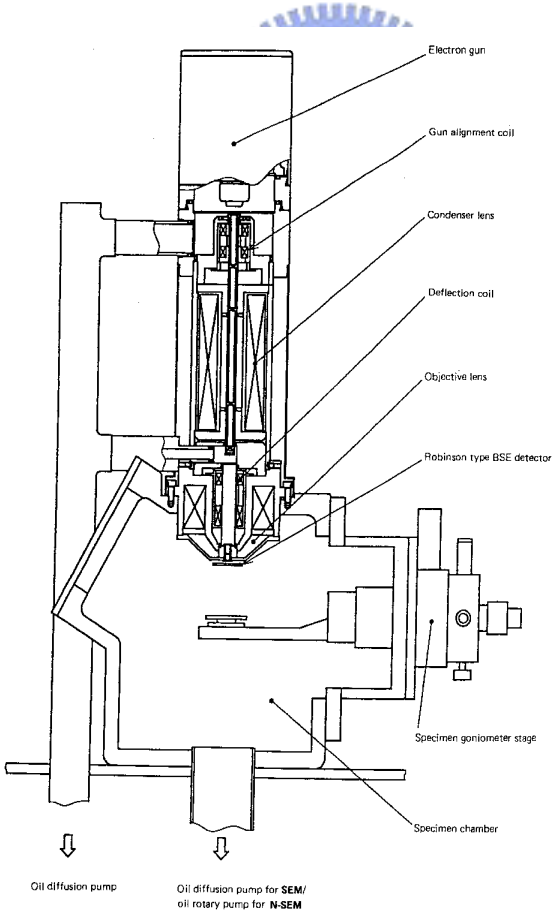


Fig. 3-2 Schematic diagram of the EB control system.


Fig. 3-3 SEM

For our experiments we use electron-beam lithography (EBL) to create pinning centers, which are comparable in size to the characteristic length scales in a superconductor. It is a convenient tool to pattern films, because the EB process does not use a photo mask. Only the pattern is designed and stored in computer which can be changed or modified rapidly. In most cases the pinning centers consisted of small dots or holes, therefore the process to make these small defects will be presented in detail.

The hole array are made by a lift-off process which is illustrated in Figure 3.1. Firstly, Au bonding pads were prepatterned onto a SiN-coated silicon substrate by optical lithography and thermal evaporation through a standard lift-off process. The bonding pad consists of 24-probes as electrode metal, as shown in Fig.3-4. Then the pattern is defined in the central area of bonding pad.

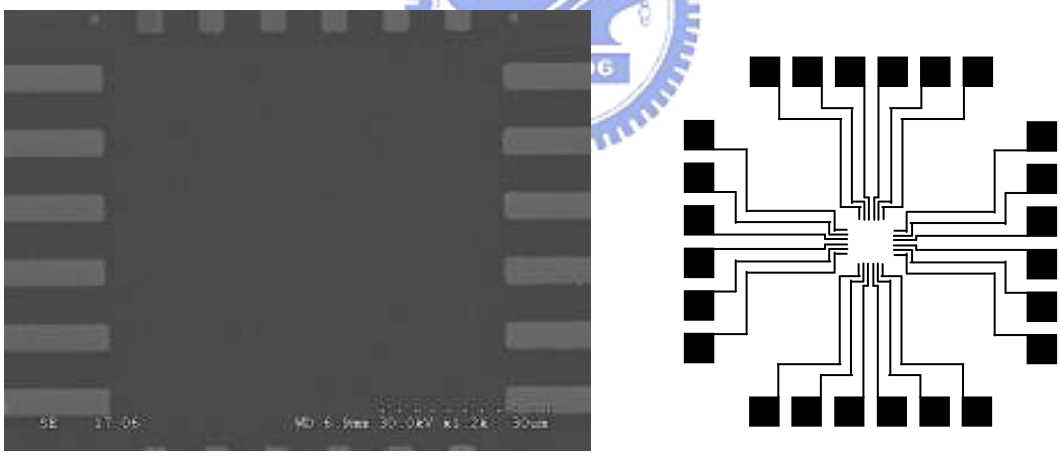

**Fig. 3-4 Bonding pads were defined by photo lithography and Au was thermally evaporated onto a SiN-coated silicon substrate. We used these patterned structures as starting electrodes in the present method.**

Secondly, a 8% solution of PMMA is spun on top of the substrate at 6000 rpm for 60 sec. The substrate is typically a SiN-coated Si substrate with (100) orientation. The PMMA is then baked at $160^0C$ for at least 2 hours. This is above the glass temperature of the PMMA ($\approx 120^0C$) and thus after this baking step, the PMMA forms a smooth film on top of the substrate. The thickness of the resulting PMMA layer is around 400 nm.

The substrate covered with the PMMA is then loaded into a scanning electron microscope; which is equipped with a Nanometer Pattern Generation System (NPGS). This NPGS provide a friendly environment to defined pattern with the electron beam of the SEM. Patterns are created using DesignCAD which is a commercial computer-aided-design program. A Hitachi S2460N scanning electron microscope with a maximum acceleration voltage of 30 kV equipped with a versatile pattern generator was used in our experiments. For the electron-beam lithography the SEM is operated at an acceleration voltage of 30 kV. After the SEM is adjusted by focusing on small gold clusters, the electron beam needs to be focused on the substrate with the PMMA.

The PMMA is then exposed to the electron beam, while the sample current is monitored. Thereafter the PMMA is right in the focus of the electron beam; the beam will break the long polymer chains of the PMMA into shorter fragments. After the pattern is defined by the exposure to the electron beam, the PMMA is developed. The parts of the PMMA with the short polymer chains can then be selectively dissolved by a suited developer. For developing, PMMA was removed in a 1:3 mixture of methyl isobutyl keton (MIBK) and 2-propanol (IPA). This solution needs to be maintained at $25^0C$ during the developing process. After developing the sample for 80 sec, the sample is then rinsed 20 sec in IPA and left a trench in PMMA. Due to the back scattering of electrons from the substrate, this PMMA stencil has a natural undercut.

Prior to the development of this procedure, it was known that this PMMA resist can be patterned as a mask. We can then either deposit patterned films or etch the substrate by dry etching. In last step of lithography is the lift-off process. In this step the remaining PMMA is removed together with the thin film that is grown on top of the PMMA if we use any standard deposition method. In this thesis the PMMA acts as a stop mask for the etching of the $Si_3N_4$ layer by RIE. Thus, the pattern of the trench in PMMA was transferred onto the $Si_3N_4$ film. The detail process of reactive etching is described in Section 3-1-2. After lift-off process, a regular array of hole left in the $Si_3N_4$ film in the central part of the bonding pad.

Furthermore, electron beam lithography was again used to open a four-robe bridge shape trench in PMMA, in which care was taken to align the hole array sitting in the center part of the four-probe bridge trench. In addition, the four-probe bridge is made to connect with the electrode metal of bonding pad. Then, Niobium film of about 100 nm was dc sputtered onto the patterned substrate. This detail for this growth is described in Section 3-1-3.

## 3-1-2 Etching

After the trenches in PMMA were defined using EBL, the sample was loading into reactive ion etcher (RIE) to etch the $Si_3N_4$. The PMMA layer acts as a mask for the etching of the $Si_3N_4$ layer.

This RIE system is equipped with a main chamber and a turbo-pump. In general, the chamber should be evacuated to remove the air inside. Then we fill the chamber with process gases and set the base pressure of the main chamber equal 3.3 mtorr. For our sample, the sample is etched in a chamber with plasma of oxygen gas and $CF_4$ gas whose ratio is 1:8. After the chamber pressure and gas flows time is

stable, we can turn on the RF power and set the time to 3 min. It is noted that the main RF power at the distribution board should keep at stable operating value of 220 V and diminish the reflected power. Usually, we do all above procedure before we are loading the sample. The etching rate for these parameters is 20 nm/min.

In order to remove the PMMA, the sample is soaked in acetone for 15 minutes and then agitate sample in acetone with an ultrasonic cleaner for additional ten seconds to complete the lift-off. Finally, rinse in IPA and then blow dry with nitrogen gas. In a final step of the etching the sample is cleaned again in RIE. This time we clean in a chamber with plasma of oxygen gas for several minute. The pattern is then checked under an atomic force microscope (AFM) and in the scanning electron microscope (SEM). A scanning electron micrograph with a particular pattern of hole array in $Si_3N_4$ is shown in Fig. 3-5. In this case the hole diameter is 200 nm and the separation of the hole is 500 nm.

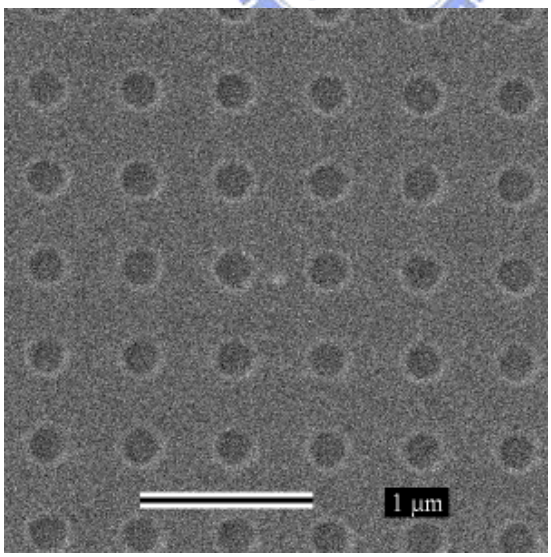


**Figure 3-5. Scanning electron micrograph of a SiN-coated silicon substrate with holes. The holes are 200 nm in diameter and positioned on a square lattice with a lattice constant equal 500nm. The scale is given at the bottom of the picture.**

### 3-1-3 Film growth and characterization

For the preparation of the sample, it is generally necessary to deposit superconducting film. The niobium film used in the thesis is grown by DC magnetron sputtering.

The sputtering system consists of a main chamber, a loading chamber and a turbo-pump, as shown in Fig. 3-6. The base pressure of the main chamber is controlled in the $10^{-8}$ Torr range. The main chamber has one sputtering gun, which is only used for superconducting study because the properties of Nb are very sensitive to impurities. Nb film of about 100 nm was dc sputtered onto the patterned substrate through a homemade collimator, which made well-defined edges of devices after the lift-off process. In order to avoid oxidization of the targets affecting the deposited film, the targets are generally presputtered for at least 9000 second. Nb is grown using dc-sputtering with a power of 40 W from a 99.98% pure Nb target at an Ar pressure of 3 mTorr for 6000 second. The growth rate for these parameters is 1/6 Å/sec. This was done to facilitate the characterization of the deposited material; in particular for determining the thickness by AFM.

The Nb films are furthermore characterized by their magnetic properties in a SQUID system. Since the thickness of some of the Nb films is comparable to the coherence length, the $T_c$ is somewhat reduced from its bulk value of 9.2 K. The transition width is generally a better indication of film quality. Normally the transition width is $\Delta T_c$=0.1K or less. A higher transition width can indicate impurities in the sampes or in homogeneities in the film thickness, so that the $T_c$ varies locally. Another good indicator of the Nb film quality is the normal state resistivity. Figure 3-7 shows cross-section of the niobium film. This indicated the Nb film is continued all over the film plane.

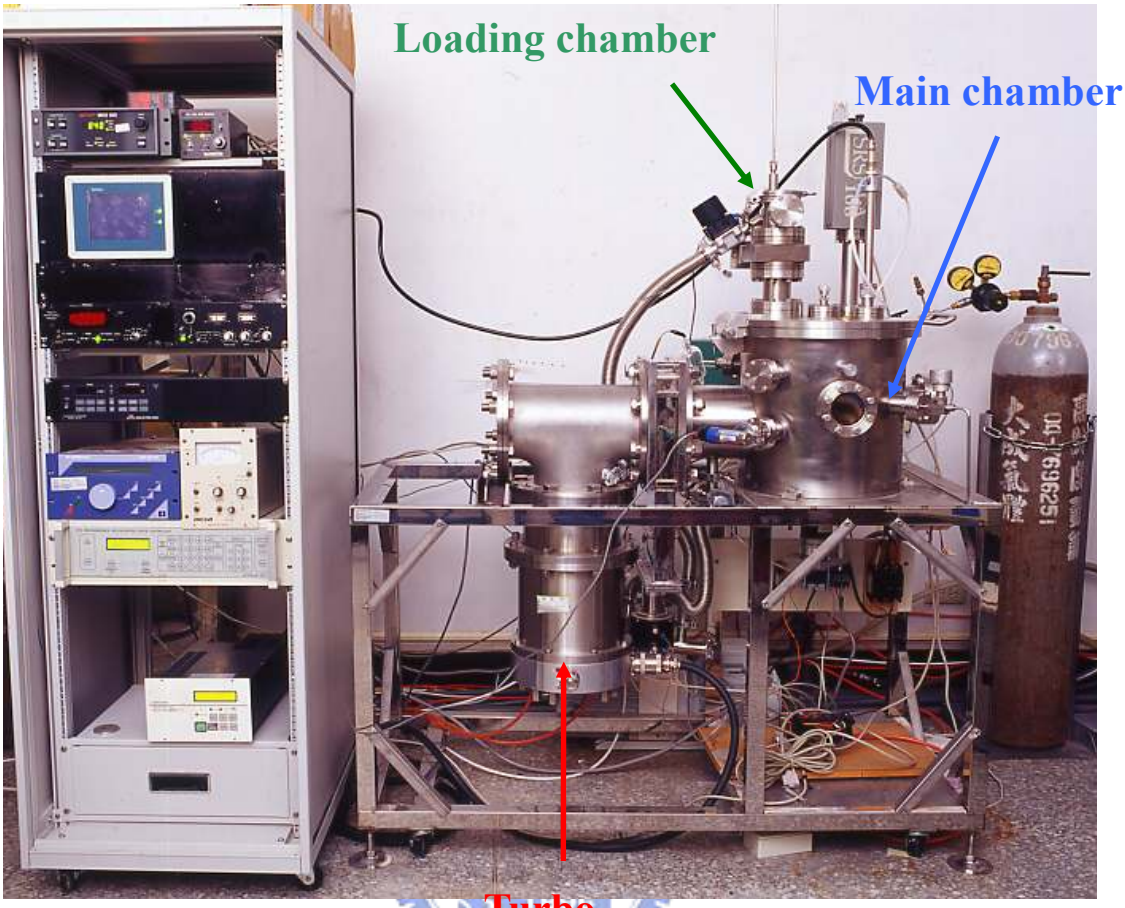


Fig. 3-6 Dc sputtering system

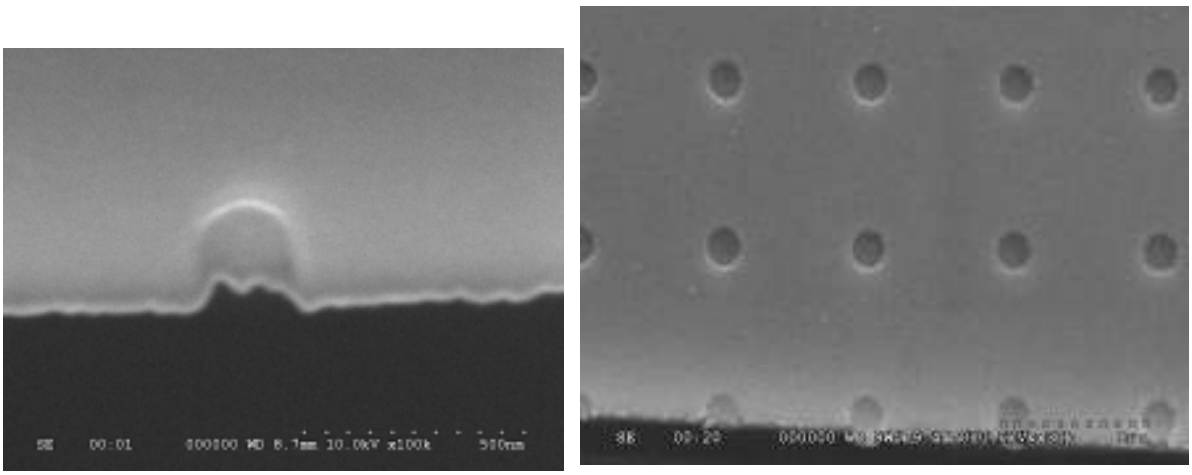

Fig. 3-7 Cross section of the niobium film

## 3-2 Measurements

Most of the measurements of the Nb films with dots were transport properties in a SQUID system. The details of these transport measurements are described in Section 3-2-1. In addition, AFM image were used to measure the depth of the films.

### 3-2-1 Transport measurements

Transport measurements are performed using the measurement bridges described in Section 3-1-3. The sample is glued to the probe and then inserted into a SQUID system. The SQUID system is a quantum design model MPMS-5S with a low temperature fluctuation within 3 mK. The SQUID system is a helium bath cryostat capable of maintaining sample temperatures between 2 and 400 K. It is equipped with a superconducting solenoid, thus the external magnetic field is applied vertical and ranged from -5T to 5T. The sample was place in the center of the solenoid and the external magnetic field was always applied perpendicular to the plane of film.

One crucial problem during most of the measurements is that they are made at a temperature very close to the critical temperature. Since the physical properties of the superconductor change drastically with temperature at these temperatures it is very important to keep the temperature during the measurement very stable.

The magnetoresistance of our films is measured by the standard four-probe technique, using a current source (for dc current source is Keithley 220 and for ac current source is lockin amplifier) and a nanovoltmeter (Keithley 182). A PC is used to collect the data and to control a switchbox to switch between several samples. The PC also records the measurement temperature and sets and records the applied magnetic fields.

For the transport measurements shown in Chapter 4 it are necessary to apply a

current above the critical current. At the same time the measurement current cannot exceed the critical current by too much, since these results in driving the ample into the normal state. This limits the measurements to a very small temperature range (typically 0.1-0.5K) just below $T_c$. The current density, and thus the critical current density, has to be below 100 $kA/cm^2$ (corresponding to a few mA in a typical sample) to avoid significant sample heating.

The critical current is determined form I(V) curves, which are again recorded by the PC using different DC current. In order to get rid of any offset voltage the measurements foe negative and positive current are averaged. Generally the critical current is determiner in the literature by the applied electrical current, which results in a non-zero voltage defined by an electrical field of 1 $\mu V/cm$.

**Fig. 3-8 SQUID system**

### 3-2-2 Atomic force microscopy

For magnetic force microscopy one needs a mechanical cantilever which has a ferromagnetic tip. This is normally fabricated by coating the tip of a commercially available cantilever for an atomic force microscope (AFM) which a thin ferromagnetic film.

An AFM has the same basic design as a MFM, only it has a non-magnetic tip on its cantilever. This was done in order to quantify the corrugation of the Nb films grown on top of the holes. From the topographic data from the AFM data, this is very good smoothness of the films.

**Fig. 3-9 AFM**

# Chapter 4

# Results and discussion

---

This dissertation is devoted to the study of the vortex pinning properties of the hole array. In this chapter, all the experimental results will be presented in detail. In addition, before going through the main subjects, the effects of regular array of pinning sites are first reviewed (see Section 4-1). We describe the basic effect of a periodic array of holes on the transport properties of a superconducting Nb film. Moreover, the influence of the geometry of the hole array is discussed (see Section 4-2). We will show three different kinds of geometry of hole array. Furthermore, the asymmetric properties of triangular array of pinning sites are compared on the directions of vortex motion (see Section 4-3). Then we get into the main subject concerning with the pinning effect of spacing-graded of pinning sites (see Section 4-4).

## 4-1 Basic periodic pinning

### 4-1-1 Results of square array of pinning sites [37, 38]

The effect of the ordered array of structural corrugations on the vortex motion is clearly present in the mixed state of the Nb film. A geometric matching of the vortex lattice with a periodic pinning array can lead to an enhancement of the vortex pinning. In this section we will illustrate the pronounced effect and give a brief discussion. Notice that the magnetic field is always applied perpendicular to plane of the superconducting Nb thin film for all the measurements presented throughout this thesis. Figure 4-1 shows the simultaneous measurements of the magnetoresistance

(MR) curve and critical current Ic(H) as a function of applied magnetic field for a Nb thin film with a square array of defects at T/Tc=0.984. The sample has 100 nm thick Nb film covering 60nm depth holes with a diameter of 300nm. The holes are arranged on regular square lattice with a lattice constant of a=500nm. The MR curve and Ic(H) curve are measured at T=8.75K, which is just slightly blow the critical temperature of this film.

For MR curves, the measurement is made with a current of 100 $\mu$A, which is just above the critical current at this temperature. As shown in Fig. 4-1, there is a set of minima in the MR curve at periodic magnetic field values. This is different from what is observed for a reference Nb thin film, which presents the usual monotonic increase in the resistance with the increasing applied field. The periodicity of these peaks is $\Delta H = 91.2Oe$, which corresponds to a vortex density

$$n_v = B/\Phi_0 = 4.4\times10^8 cm^{-2}.$$

This is in agreement with the pinning centers density

$$n_p = 1/(500nm\times500nm) = 4.0\times10^8 cm^{-2}$$

of the square hole array. This corresponds reasonably well to the matching field $H_1$. This implies that the defects in the artificial regular array due to structural corrugation in the Nb thin film act as very strong pinning centers and dip appears at matching fields in which there is an integer number of vortices per unit cell of the regular array of defects.

For Ic(H) curve, similar periodic peaks can also be observed in the measurements of the critical current as a function of applied magnetic field. The maxima in the critical current density occur at exactly the same magnetic field as the minima in the MR curve. Thus the periodicity for the peaks in the critical current is also $\Delta H = 91.2Oe$. Again this is in contrast to an ordinary type II superconductor,

where the critical current decreases monotonically with increasing applied magnetic field.

Figure 4-2 shows the IV curves at integer and half-half-integer matching fields. At higher driving force an ordinary monotonic behavior can be observed, that is, the voltage drop increases with magnetic field. However, at lower driving force a distinct crossover is observed in that the voltage drop at integer matching fields becomes smaller than that at half-integer ones. A crossover occurs for currents exceeding a certain threshold value. In the low current density region, the vortices tend to form a triangle lattice easily at matching field that the vortex lattice configuration can sustain the driving force with less energy loss. In the high current density region, however, the vortex lattice configuration cannot hold in the higher driving force.

For the observed crossover form the IV curves, these peaks in the resistivity can be observed over a wide range of applied current densities. This is also shown in Figure 4-3, where the magnetoresistance measured at the same temperature is plotted for several different current densities in a limited current range 10-300 mA. As can be seen, all these curves show the same minima in the MR curves at equal matching field. Vortices are bound elastically to the pining centers and form some geometric configurations at matching fields regardless of the magnitude of applied force. The magnitude of applied force does not change the periodic matching field. A strong pinning effect and matching effect can be found in the sample under the influence of the underingly array structure in the superconducting Nb thin film.

This section discussed so far is introduced the matching field. This matching effect exists in all samples with periodic pinning centers in the superconducting films. However, there is no careful comparison of the matching effects in samples with different separation or different lattice geometry of the hole array. Some of the measurements presents in this section simply point out the matching effect is indeed

related to the interaction between vortex lattice and the regular array of defects. As a result, there are no matching effects in the as grown film and the transition width and the normal state resistivity are fairly small.

This matching effect has been indeed directly observed by Harada et al. [21]. for a Nb thin film sample. In their experiments a regular square array of defect was prepared using a focused 30 kVGa ion beam. In this sample the positions of the vortices were observed directly using Lorentz microscopy. The vortex positions of the vortices were observed directly using Lorentz microscopy. The vortex positions observed in these experiments were very well reproduced by subsequent numerical simulations of vortices in regular pinning arrays by Reichhardt et al. [22], whose results are shown in Figure 2-2.

Aside from interstitial vortices, another possibility is that the artificial pinning centers can either pin several vortices or that even multiquanta vortices can be stabilized at these pinning centers. For an isolated pinning center with a diameter d the saturation number $n_s$ of flux quanta $\Phi_0$ which a pinned vortex can support is $n_s \cong d/[2\xi(T)]$ [23].

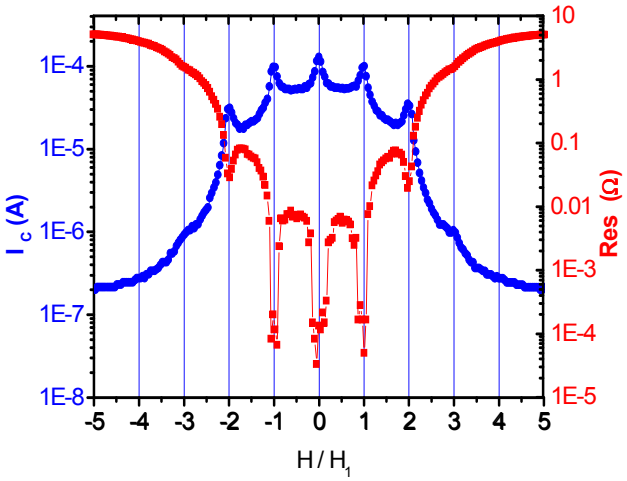


**Fig. 4-1 Field dependence of the resistance and critical current for a Nb film with a square array of defects at T=8.75 K.**

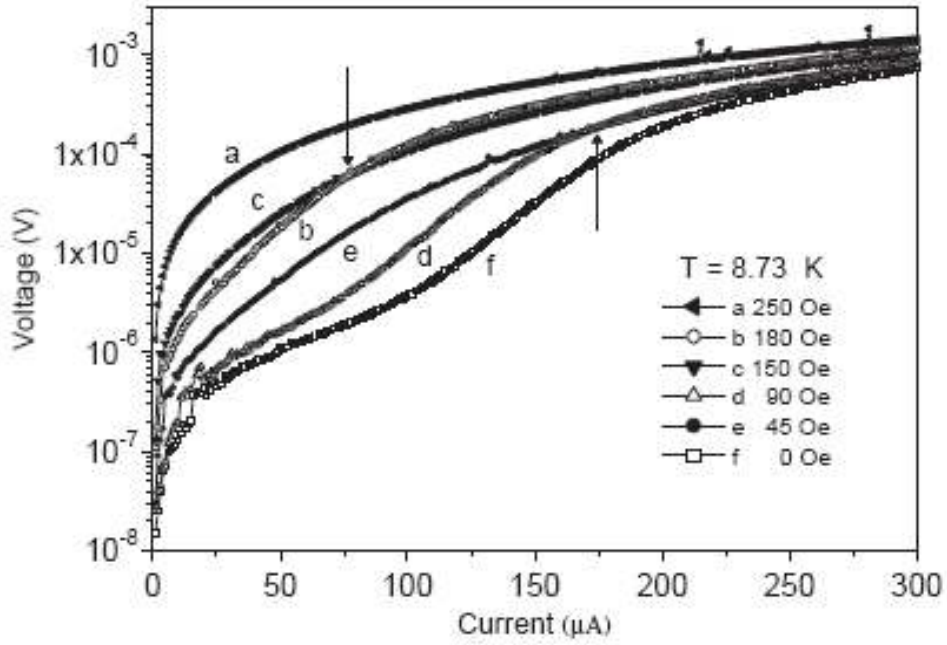


**Fig. 4-2 I – V characteristics for a triangle lattice at T=8.73 K under various magnetic fields applied perpendicular to the film plane. The arrows represent the crossover currents between integer and half-integer matching fields.**

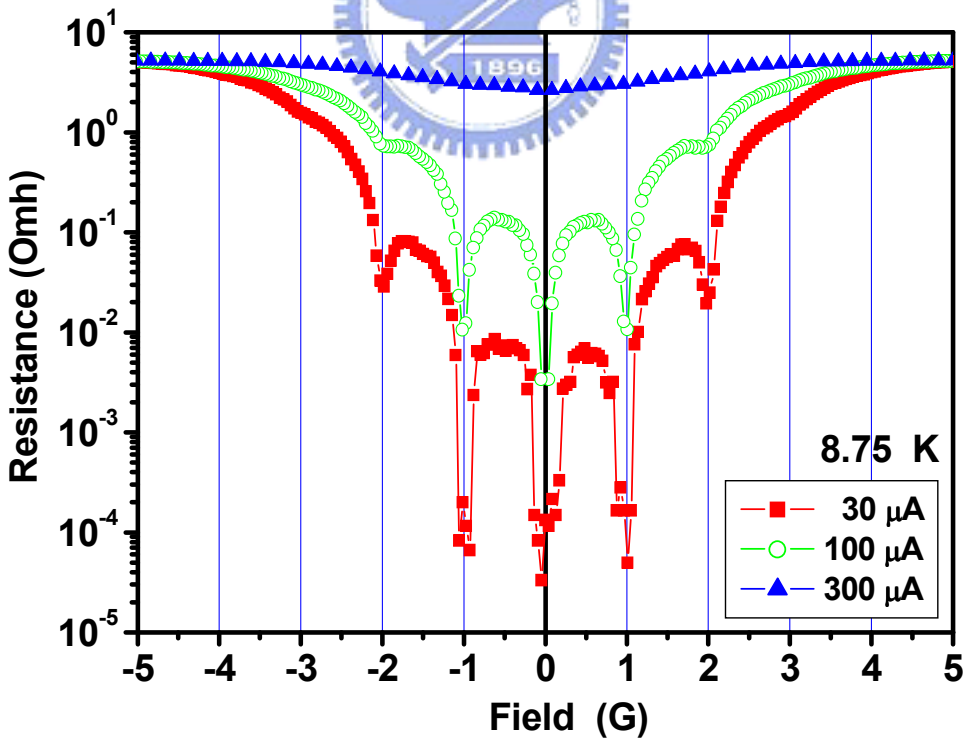


**Fig. 4-3 Magnetoresistance for different injected current in a Nb film with a square array of defects at T=8.75 K.**

## 4-1-2 Periodic Pinning basics

As was shown in this section, Nb films with periodic pinning arrays consisting of holes, show matching effects in the magnetic field dependence of the resistivity and the critical current density. The magnetic fields at which these matching effects occur can be very well described in terms of matching fields ($H_n$); which only depend on the density of pinning centers. The results can be explained by the numerical simulations of vortices in regular arrays by Reichhardt et al. [22], whose results are shown in Section 2-3. In addition, this can be clearly seen in the way that the matching fields Hn vary for diffident geometries of the pinning center arrays; which have different pinning center densities. A further discussion will be given in next section.

The experimental results with the square hole array show the matching effect in Nb. This basic principle of the matching effects in superconductors with periodic pinning is fairly simple. Since the Nb is generally grown on top of the hole, the corrugation of the Nb film plays an important role in pinning the vortices. One possibility to explain this result is that the holes reduced the thickness of the Nb films. Thus the corrugation of the Nb films due to the holes may lead to a locally depressed critical temperature along the perimeter of the holes. Since all the measurements are done very close to the critical temperature, this locally reduced critical temperature can give rise to a normal conducting region in which the vortices can be pinned.

Besides the above mentioned pinning mechanism caused by the film corrugation, the effect of the vortex pinning by the pinning sites was also studied by several groups by using magnetic dots. The dots array also caused the corrugation of the Nb. However, the periodic pinning effects are more pronounced for the samples with magnetic dots. There are several pinning mechanisms being considered from the magnetism of the magnetic materials. They are the stray field of the magnetic dot (in-plane magnetization) [39-42], high magnetic permeability of the dot (out-of-plane

magnetization) [41-43], and ferromagnetic proximity effect [44].

Before discussing these in detail, the experimental results presented in this thesis are compared to data obtained from other groups working on similar systems. Several groups made measurements of superconductors with periodic arrays of magnetic dots. J. I. Martin et al. made much effort on pinning effects on Nb films with the periodic arrays of magnetic dots. [45, 46] Some of the details, like the pinning mechanism and the geometry of the vortex array at higher order matching fields are more complicated than our results.

The periodic pinning effects are more pronounced for the samples with magnetic dots and shows more peaks than that for non-magnetic dots and holes in the Ic(H) curves and dips in the MR curves. This is also consistent with the measurements shown in their paper where the matching effects are more pronounced for the samples with Ni dots compared to the ones with Ag dots. Furthermore, these curves are independent of the magnetic history of the dot array. The lack of hystersis in the interaction of the magnetic array and the superconducting film indicates that the stray field from the magnetic dots does not play a crucial role.

L. Van Look et al. studied flux pinning in thin superconducting Pb films covering a triangular array of magnetic Au/Co/Au dots with in-plane magnetization. [41] The same results also get from Van Bael et al. [42] The array of magnetic Co dots is prepared by electron-beam evaporation. According to topography of the magnetic dot array from magnetic force microscopy (MFM), two kinds of states can be found in the magnetic dots. One is the multi-domain state in the as-grown dots, and the other is the remanent single-domain state with a magnetic moment oriented along the direction of the magnetic field used for the saturation. Figure 4-4 the bright and dark spots indicate a positive and negative z component of the stray field, with respectively.

Figure 4-5 shows the critical current density as function of magnetic field for the single-domain and the multi-domain state of the dots. Both samples show clear peaks at matching fields and the matching effects are enhanced for the magnetized Au/Co/Au dots compared to the non-magnetized dots. That is, there is an overall enhancement of critical current in the case of the single-domain state compared to the multi-domain case. This clearly indicates that a strong pinning of the vortex lattice for single-domain case. Furthermore, the Ic(H) curves is independent of the magnetic history of the dot array. This is because vortices are pinned at bright spots for positive magnetic field, while vortices are pinned at dark spots for negative magnetic field. In other words, the domain structure for the stray field from the Co dots is symmetry for the vortex. This suggests that the magnetic stray field of the magnetic dots influences the pinning of the vortices, since the magnetic stray field should be bigger for single domain dots than for dot with multiple domains. The increase of the stray field strength enhanced the pinning efficiency on the pinning potential.

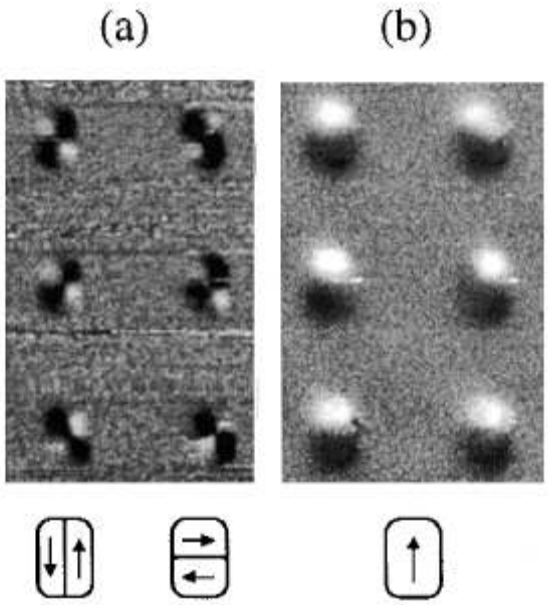


**Fig. 4-4 Magnetic force micrograph of a square lattice of submicron magnetic dot (a) before magnetization, and after magnetization along axis of the dots. Adapted from Ref. [41].**

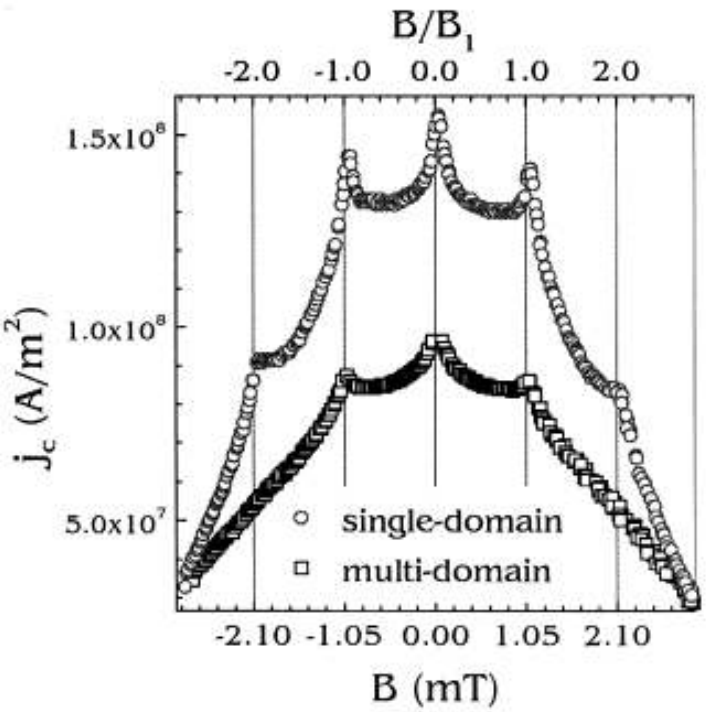


**Fig. 4-5 Critical current density in function of magnetic field at T/Tc=0.985 for a superconducting film covering the triangular magnetic dot array in the single-domain and in the multi-domain state. Adapted from Ref. [41].**

Besides using in-plane magnetization of dots there have been some studies which use out-of-plane magnetization of the dot as artificial pinning centers. The experimental results have strict difference for the pinning properties. Margriet J. Van Bael et al. studied the pinning effect on superconducting Pb film with square array of Co/Pt dots as a magnetic pinning array which is with out-out-plane magnetization [43]. The magnetic dots are consist of multi-layers which are Pt(64Å)/[Co(5Å)/Pt(16Å)]$_{10}$. In this sample the vortex lattice in a perpendicular applied field can interact with the perpendicular magnetic moment of the Co/Pt dots.

In order to investigate the interaction between the vortex and the perpendicular moment of the Co/Pt dots, the positive and negative magnetization were studied in the remanent state after saturation in a positive (negative) perpendicular [47]. Then the most of the dots will have a positive (negative) perpendicular field. According to the MFM image we can get either dark or bright spots which are defined by the stray field of the MFM tip. The dark and bright spots are indicating a single-domain structure with out-out-plane magnetization. Figure 4-6 shows the resulting hysteresis loops with the dots magnetized in a positive and a negative perpendicular field. A pronounced asymmetry of the H>0 and H<0 parts can be observed in both M(H) loops. These curves are dependent of the magnetic history of the dot array and asymmetrical with respect to the field polarity. Clear matching effects are only observed in that part of the curve where the field polarity is aligned parallel with m of the dots.

The polarity-dependent flux pinning effect of the magnetic are due to the mutual orientation between the out-out-plane magnetization of the magnetic dots and the magnetic field applied perpendicular to the film. The magnetic dot can produce an attractive pinning potential when H is parallel to the magnetic moment of the dot and repulsive when H is anti-parallel to it. This indicates that a lattice of dots m>0

provides a much stronger periodic pinning potential for positive vortex lattice compared to dots with m<0, and vice versa.

Q. H. Chen et al. [48] simulated interesting pinning properties of the vortex dynamics in the superconducting film with ferromagnetic and anti-ferromagnetic arrays of magnetic dots, as shown in Fig. 4-7. Three kinds of magnetic dot arrays, FM, AFM, and AFM2×2 were investigated. By taking advantage of the field polarity-dependent pinning effect, the author tuned pinning from asymmetric (FM) to symmetric (AFM and AFM2×2) with pronounced matching effects. Their results are similar to the former results. For FM configuration, the vortices are strongly pinned at the pinning sites at H>0. The anti-vortices, however, are repelled by the dots, and are caged at the interstitial position. Interestingly, for the AFM and AFM2×2 configurations, the vortices are pinned at the up-magnetized dots at H>0, while at H<0 the anti-vortices are pinned at the down-magnetized dots. Hence, the observed symmetrical behavior has a rather straightforward.

From the observed matching effects in the pervious papers, it is clear that the pinning mechanism can get involved in the corrugation of the superconducting film, the stray field of the magnetic dots, the high magnetic permeability, or proximity effect. But the actual pinning mechanism can be one of those or more.

### 4-1-3 Pinning mechanism

From the observed matching effects it is clear that the Ni dots and the Ag dots act as pinning centers for the vortices. The mechanism that pins the vortices is a priori not necessarily obvious. The initial motivation of using magnetic dots as pinning center was to pin the vortices due to magnetic interactions. However, since the Nb is generally grown on top of the magnetic dots the corrugation fo the Nb film may also

play a role in pinning the vortices.

In fact, the observed matching effects for samples with Ag dots suggest that the corrugation of the Nb films is not negligible. The main effect of the corrugation is that the Nb film effectively has a reduced thickness along the perimeter of the dot. This reduced thickness along the perimeter of the dot. This reduced thickness can pin a vortex since the loss in condensation energy due to the normal conducting vortex core, in minimized; if the vortex is positioned at the constriction of the superconducting film. Furthermore, in the Nb films used for the experiments in this thesis, the critical temperature depends on the film thickness. Thus the corrugation of the Nb film due to the dots may lead to a locally depressed critical temperature along the perimeter of the dots. Since all the measurements are done very close to the critical temperature, this locally reduced critical temperature can give rise to a normal conducing region in which the vortices can be pinned. Indeed, the first measurements of vortex matching effects in type II superconductors were done in granular Al films with periodic thickness modulations.

The effect of corrugation in the superconducting film on the vortex pinning was also studied by Filby [49]. These samples consist of 60 nm thick Pb films deposited through a template of spheres with a regular array of holes. One would expect that the corrugation of these Nb films on top of the template with holes is comparable to the corrugation of Nb films deposited on top of dots. All these samples show periodic pinning effects. The differences in commensurability behavior are because of the spherical shape of the pores. The spherical shape gives rise to a smoothly varying pinning potential resulting in significantly smaller critical current than in the case of structures with relatively steep-edged holes.

Although there are periodic pinning effects for some of the samples with non-magnetic dots, the comparison of the data for samples with Ni and Ag dots shows

that the periodic pinning effects are more pronounced for the samples with magnetic Ni dots. Furthermore, for the above mentioned pinning mechanism caused by the film corrugation, one would expect that any pinning due to the corrugation will be diminished for thicker superconducting films, when the ratio of the film thickness to the dot thickness increases. However, there is at most only a very weak dependence of the periodic pinning on the superconducting film thickness. This strongly suggests that the magnetism of the Ni dots plays an important role for the pinning of the vortices. There are several different possibilities as to how the magnetism of the Ni dots can lead to a pinning of the vortices. Nozaki et al. suggested that the stray field of the magnetic dots can locally suppress superconductivity. One would therefore expect that the pinning depends on the magnetic history of the ferromagnetic dots; which is in deed what several groups observed. However, the measurements presented in this thesis are independent of the magnetic history of the samples and do not show andy hysteresis. Consequently it is unlikely that the stray field influences the pinning in these samples. This is further supported by the absence of any matching effects for the samples with Ni dots on top of the Nb film.

It is possible that the ferromagnetic dots due to their high magnetic permeability concentrate the magnetic field at their location and thus the vortices are preferably located at the position of the dots. However this mechanism is again difficult to reconcile with the experimental result, in that there are no matching effects with Ni dots on top of the Nb. Another possible pinning mechanism is that the dots due to a ferromagnetic proximity effect suppress locally superconductivity around the magnetic dot. In this case the transfer of spin polarizes electrons from the ferromagnet give rise to pair-breaking the superconductor. Generally such a proximity effect requires a very good contact between the superconductor and the ferromagnetic material. However, the sample preparation is not necessarily conductive to preparing

such a clean interface. In spite of this, pinning due to a proximity effect may explain the difference between the samples with the Ni dots underneath and those on top of the Nb film. As mentioned in Section 3-1-1 a degradation of the Nb is unavoidable when the Ni dots are prepared on top of the Nb film. This degradation is most likely due to oxidation of the surface of the Nb film. This oxidation would limit any proximity effect between the Ni dots and the Nb film and may therefore explain the absence of matching effects for the Nb films with Ni dots on their surface.

Besides these magnetic pinning mechanisms there is also a possibility, that superconductivity in the Nb on top of the Ni dots is suppressed due to growth related problems. This is of course difficult to distinguish from a similar suppression of superconductivity due to a proximity effect.

At this point the exact pinning mechanism remains speculative. Further insight into this pinning mechanism could be obtained if the position of a pined vortex with respect to the dot could be determined. In the case that the corrugation of the Nb film or the stray field of the magnetic dots dominates the pinning, the vortices should be located at the edge of the dots. Conversely, if the pinning is due to the high magnetic permeability or due to a local suppression of superconductivity due to a proximity effect, one would expect the vortices to be centered at the magnetic dots. Notice that this is only true as long as there is only one vortex pinned per dot. If more than one vortex is pinned per dot, then the vortices will be attracted to the edges of the pinning centers in order to maximize the intervortex distance.

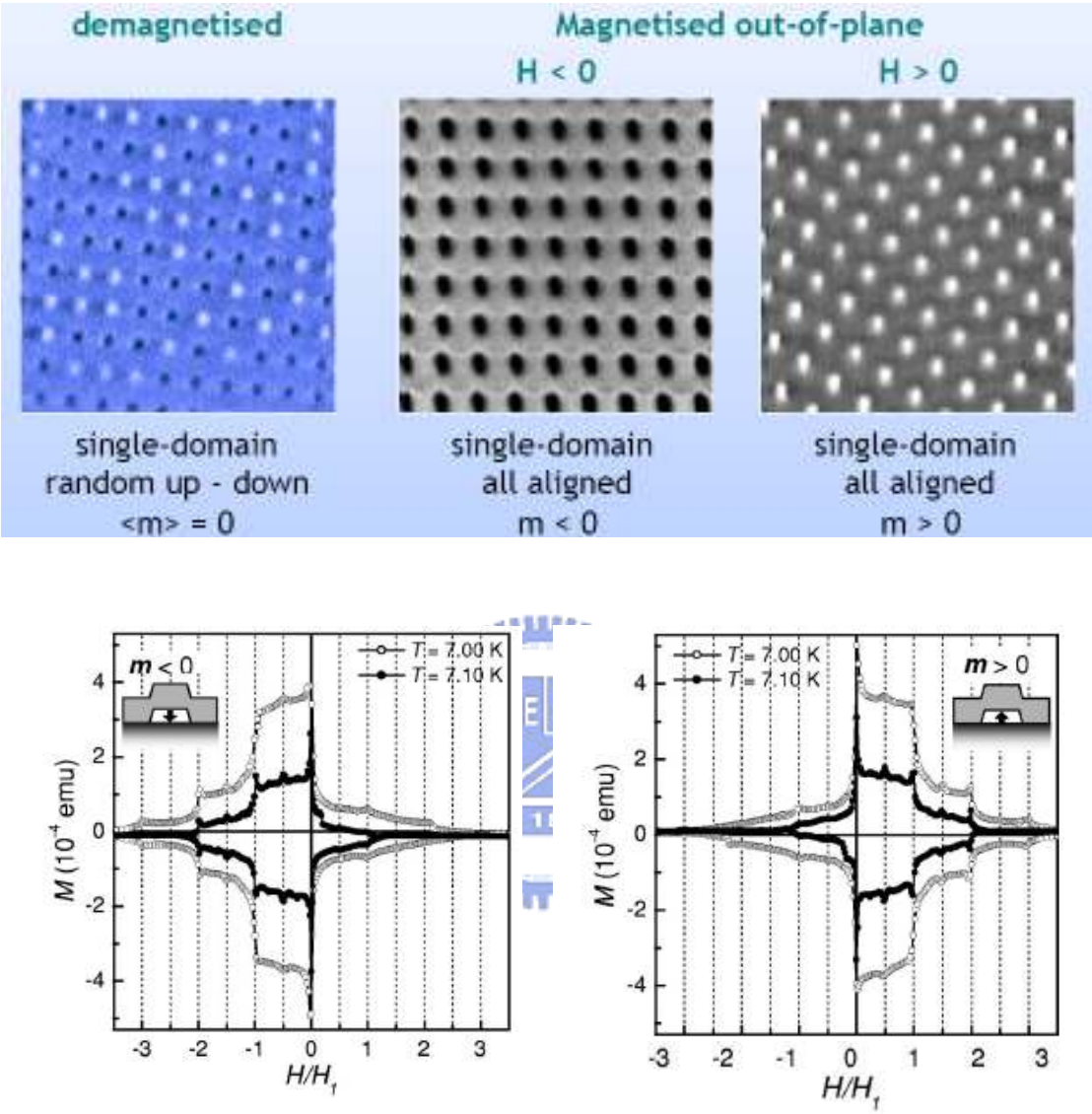


**Fig. 4-6 Critical current density in function of magnetic field showed the asymmetric properties for different magnetism. Adapted from Ref. [47].**

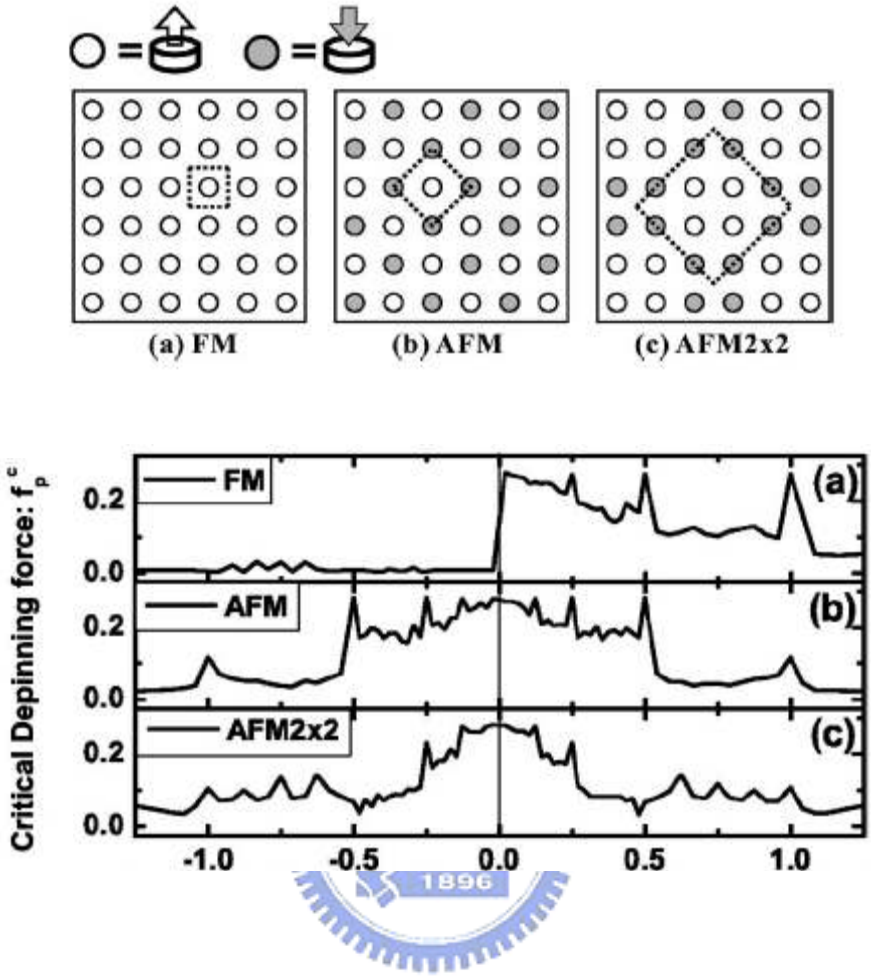


**FIG. 4-7. Three configurations of the magnetic dot arrays used in our simulation: (a) FM, (b) AFM, and (c) AFM2×2. The black open and gray filled circles are the up- and down-magnetized dots. The dotted lines indicate the unit cells for each configuration. Adapted from Ref. [48].**

## 4-2 Influence of lattice geometry

### (1) Regular array

As shown in the last section, the corrugation of the Nb film can be clearly seen in the SEM micrograph. Since for most of the samples the Nb film is deposited on top of the circular holes in the substrate, the possible origin for the pinning of the vortices is due to the corrugation of the Nb film. This type of holes effectively pins vortices in Nb due to the corrugation of the Nb film causing a lower Tc superconductor than other region the only Nb film. As we know vortices tend to be captured in the hole array, a series of samples was prepared with different geometry to find out the pinning strength of the pinning sites. In addition, we can find out the favorable arrangement of the vortex lattice in individual hole geometry. All of these samples have the sample lattice constant of 400nm [50-54]. Furthermore, the thickness of the Nb films is controlled equal 100nm. This guaranteed that all of the films for different sample have similar physical properties. The SEM micrographs of these hole array with Nb deposition on it are shown in Fig. 4-8. We can see the dark gray area is the position of hole and the bright area around the circular holes is the corrugation of Nb film. Among these three samples, the density of the holes per unit area is highest for the sample with triangular array of pinning sites. Then the density of the holes per unit area for square array of pinning sites is slightly lower than that for triangular array of pinning sites. Honeycomb pinning array is simply triangular lattices with a fraction of the pinning sites removed, that is, one third of the pinning sites have been eliminated in the triangular array. Clearly, the density of the holes per unit area from high to low is triangular array> square array> honeycomb array.

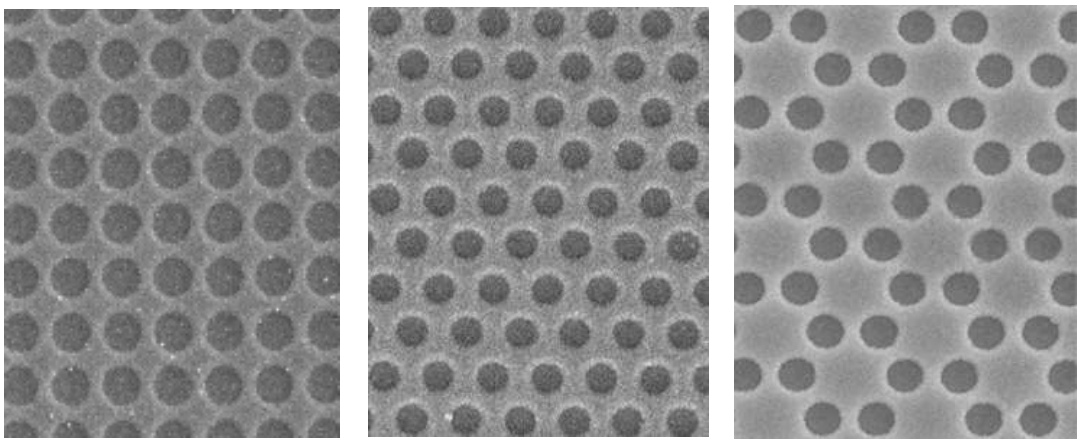

**Fig. 4-8 SEM micrographes for a Nb film with different geometries of defect array.**

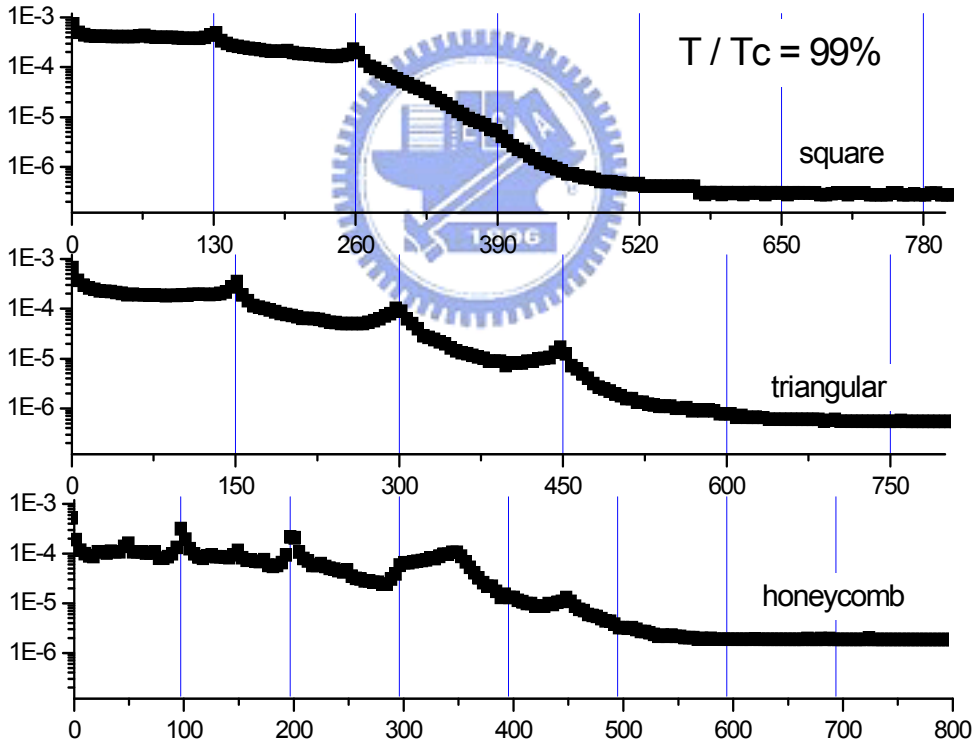


**Fig. 4-9 Critical current as a function of the magnetic field for a Nb film with different geometries of defect array.**

The magnetic field dependence of the critical current Ic(H) is shown in Figure 4-9. In order to compare all of the samples, the Ic(H) curves are chose to be measured at the same reduced temperature T/Tc=99%. The experimental data shown in this thesis shows that there are clear matching effects whenever the density of the vortices is an integer multiple of the density of artificial pinning centers. At the first matching field, where there is exactly one vortex per dot, the geometry of the vortex lattice should be exactly identical with the geometry of the hole array. Notice that the periodicity for the peaks in the Ic(H) curves from large to small is for the sample with triangular array> square array> honeycomb array. Thus the 150 Oe, 130 Oe, and 100 Oe field values can be identified as the first matching field H1, with respectively. This is consistent with the fact that the high density of hole array gives rise to high matching field for all geometry with the same lattice constant.

As seen in Figure 4-9, there are matching peaks observed for the sample with square and triangle geometries of the hole array, but overall the data for the two samples show a similar behavior in the Ic(H) curves. Therefore, there is no qualitative difference between the matching effects observed for square and hexagonal dot arrays. This is probably due to the relatively small energy difference between a triangle and square vortex lattice. In addition, the half-integer multiple of matching fields are barely seen for triangle and square array.

The results in contrast to the response of honeycomb array, where several unusual features, including pronounced peaks at both integer and half-integer multiples matching fields, are found. It is interesting that the field greater than the second matching field, the matching effects at half-integer matching fields become more prominent than those at integer matching fields.

There are large interstitial regions in the honeycomb pinning lattice. In this case there are more matching peaks observed because each large interstitial region can

capture more vortices. We conclude that the egg-carton structure clearly controls the flux pinning properties, revealing a diverse variety of vortex configurations in accordance with the imposed symmetry of the underlying pinning lattice.

## 4-3 asymmetric pinning

### 4-3-1 asymmetric pinning properties for regular arrays

As was shown in last section, we compare different geometries of periodic pinning arrays for our sample. Most of the results are successfully consist to the numerical simulations. Especially for the honeycomb array, much attention has been taken by F. M. Peeter and C. Reichhardt. Although the studies on triangular array of pinning sites is fully understand, there are still many topics concerning about vortex dynamics worth to investigate. The most important property is the anisotropic pinning. We found that the critical currents depend strongly on the current direction. This part of studies for our research is fully complete. We had many experimental results which are supported by our molecular dynamics simulations.

The geometry of triangular array allows the driving current to be applied along two directions. These two current paths can be applied with respect to the rhombic unit cells of the triangular arrays of pinning sites. Case A is for the current along the short diagonal and case B is for the current along the long diagonal direction.

Figure 4-10 shows the critical current as a function of magnetic field, Ic(H), normalized to $Ic_0 \equiv Ic\ (H=0)$, at T/Tc =0.992. The maxima of critical currents appear at matching fields for both cases. A strong anisotropy is found in the measurements of the critical currents for different current directions. When the field is equal to the first matching field, Ic(H) curves do not depend on the direction of the applied current. All vortex-vortex interactions between the vortices pinned in the defects cancel out at the

first matching field, so the depinning force of the single pinning centers (i.e., the critical current density of superconductors, is the same) as can be seen in Fig. 4-10. Once the Lorentz force exceeds the pinning forces, all vortices leave their pinning site simultaneously. This experimental result demonstrates that the pinning force of the Nb device is isotropic along both directions. However, when the applied field is departed from the first matching field, the critical current in case A is considerably enhanced to be in case B. The anisotropic pinning properties away from the first matching field are important. This may indicate that the vortices in the patterned film have a great influence, as illustrated in Fig. 4-11. In this case, the pinning potential created by triangular arrays of the pinning sites forms a clear anisotropic pinning landscape for the vortices. When the applied field is not equal to the first matching field, the vortices can generate an incommensurate row, as shown in Fig. 4-11 and expected by Ref. 54, and the vortex-vortex interaction forces will not cancel out at all. Moreover, in our sample with a triangular array of defects, the vortex-vortex interaction can give rise to the observed anisotropy in the pinning properties, and will result in vortices to easily flow along the short diagonal direction. On the other hand, the pinning potential formed by pinned vortices along the short diagonal can also create a channel to be movable for interstitial vortices, as shown in Fig. 4-11. Thus, it is favorable for these pinned and interstitial vortices to flow along the easier moving channels that were formed along the short diagonal in the unit cell under the action of the Lorentz force.

From our simulation the dynamic behaviors of the vortices are very different for case A and case B. the trajectories of the vortices foe driving force just above the critical depinning force for n=2 are shown in Fig. 4-12. The interstitial vortices are moving and the vortices at the pinning sites still persist there. For case A, the interstitial vortices are driven head-on toward vortices at the pinning sites and their movements are greatly hindered by them. The interstitial vortices for case B are

driven toward the space between the pinned vortices and their movements are less impacted by the vortices at the pinning sites and much smoother. These trajectories indicate that it is easier for interstitial vortices in case to depin and move than for case A.

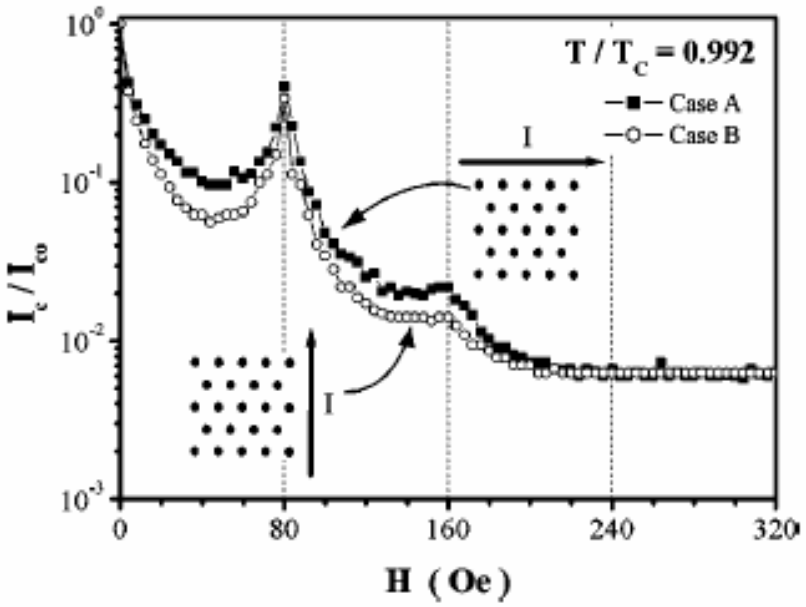


**Fig. 4-10 Critical current as a function of the magnetic field for a Nb film with a triangular array of defects.**

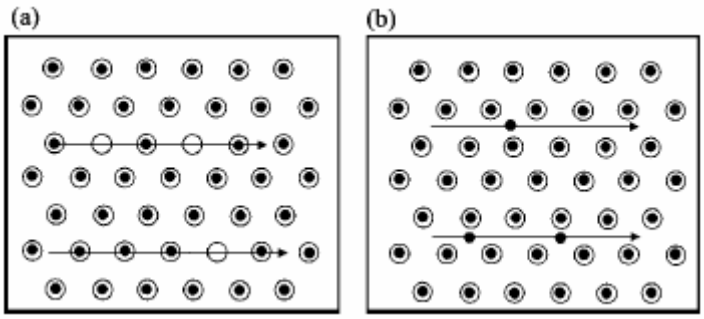


**Fig. 4-11 The vortices distribution ~filled circles! and pinning sites (open circles) for (a) the incommensurate row and (b) the interstitial flowing channel.**

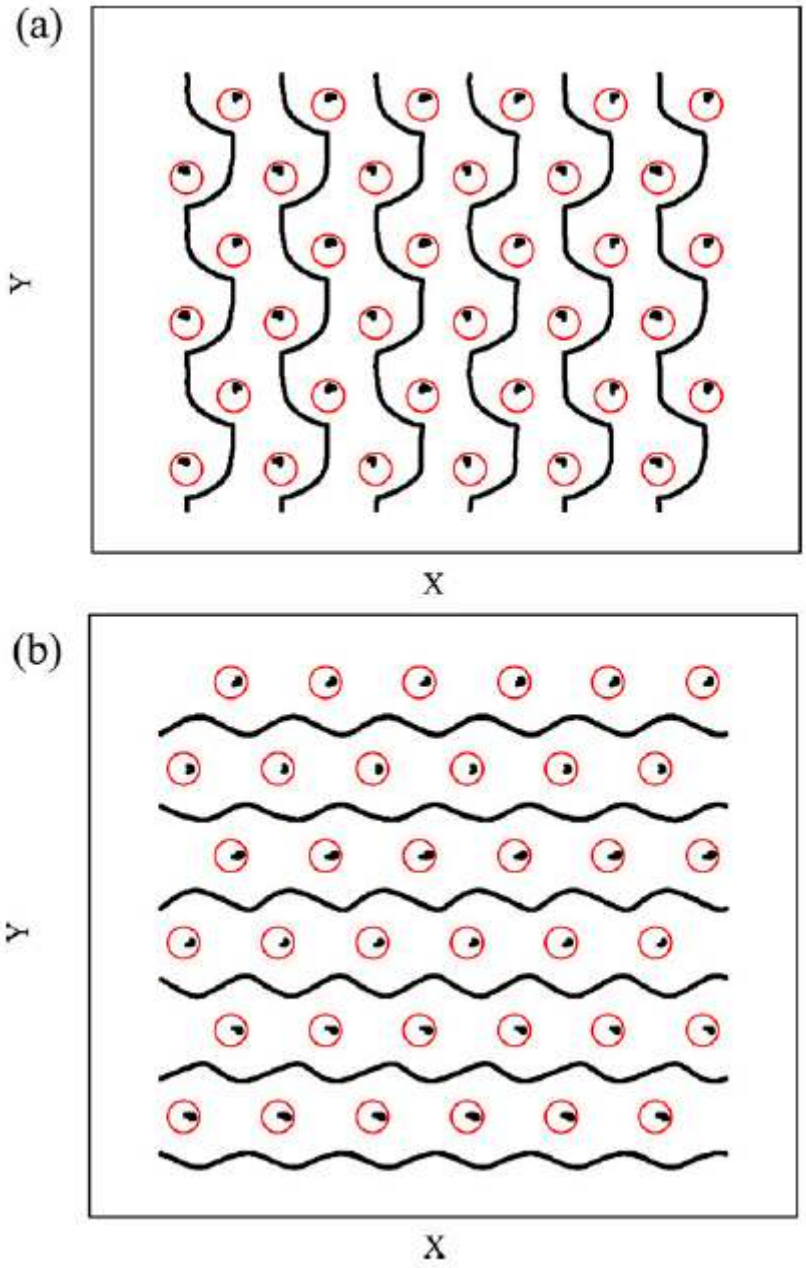


**Fig. 4-12 The trajectories of vortices for $n$ = 2 for case A (a) and case B (b) for driving force just above the critical depinning force. The open circles represent the pinning sites.**

### 4-3-2 asymmetric pinning properties for spacing-graded arrays

As seen in preceding section, the geometry of the array is all regular periodic lattices of pinning sites. The matching of vortex lattice and the artificial structure reveal a competition between the elastic energy of the vortices and pinning energy at each pinning center. As we know the most favorable arrangement for the vortices, in absence of any pinning, is triangle lattice because of mutual repulsive interaction between the vortices. We can conclude the vortex lattice is elastic, thus we can use artificial pinning center to distort the geometry of vortex lattice if the pinning energy is larger than the elastic energy. In this section, we introduce the spacing-graded array of pinning sites in the niobium films. We want to increase the elastic energy of the vortex lattice by decreasing the spacing of the pinning sites. The used samples are niobium films with spacing-graded array of holes. The lattice constant of the hole-array varied with gradient. The results obtained with this sample are directly contrasted with those measured on a reference sample, regular triangle array. In both cases, the size of samples and the number density of pinning site are the same.

The lattice-constant variation results in the change of the pinning site's density. Since the pinning strength of pinning site can balance the elasticity of vortex lattice, the vortex lattice distorts to match the hole array at matching fields. However, the commensuration effects were eliminated by introducing graded concentration of hole distributions.

Two different amounts of gradient of the hole have been fabricated, with the changing rate of the number density of defect in y-axis defined by $\Delta n_p / n_p$, where $\Delta n_p$ is the difference of the number density between the top row and bottom row and $n_p$ is the average number density. The changing rates of smaller gradient sample and the larger one are 7.96% and 69.02%, respectively.

The geometry of the holes was constructed with a constant hole separation in x-axis direction and graded separation in y-axis direction. For small gradient sample, the lattice constant increases from 392 nm to 408 nm, which the increasement started from the top row to the bottom row (see Fig. 4-14). The interval of the hole changed with an increasement of $\varepsilon$ = 0.22 nm gradually in 75 rows over the range of 30 $\mu$m along the y axis. For large gradient sample, the lattice constant increases from 326 nm to 443 nm with an increasement of $\varepsilon$ = 1 nm (see Fig. 4-15). Thus, the distance between holes would be …a-2$\varepsilon$, *a*-$\varepsilon$, *a*, *a*+$\varepsilon$, *a*+2$\varepsilon$…etc. [a = 400 nm]. The number density of the pinning sites increases gradually along y direction and is kept constant along x direction. The average number density of the pinning sites for the whole sample is equal to a regular triangular lattice of pinning sites with spacing of 400 nm (see Fig. 4-13).

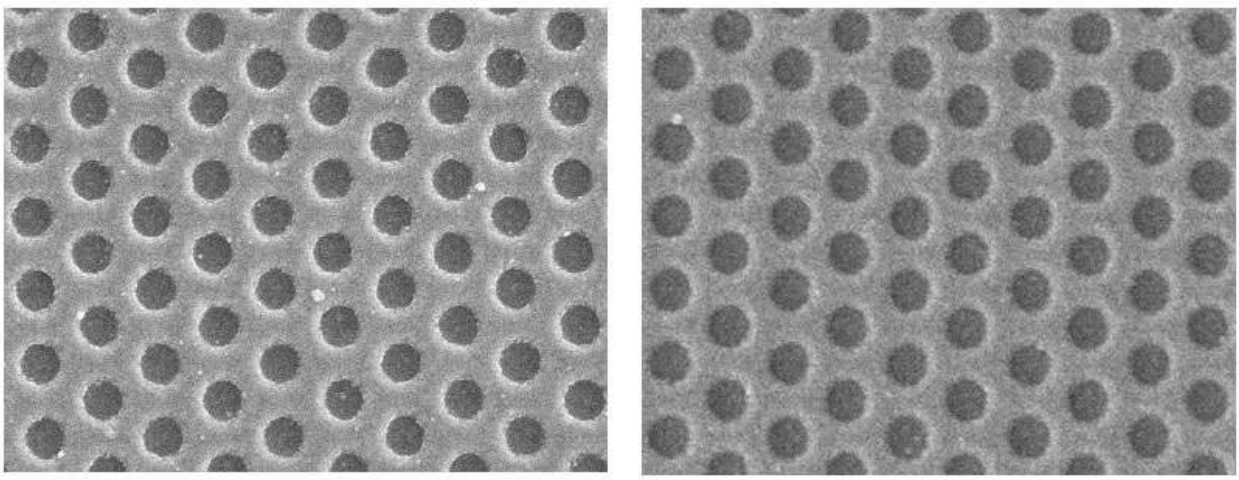

**Fig. 4-13 SEM micrograph. Sample A is triangular array of pinning sites and the sample B is graded ones.**

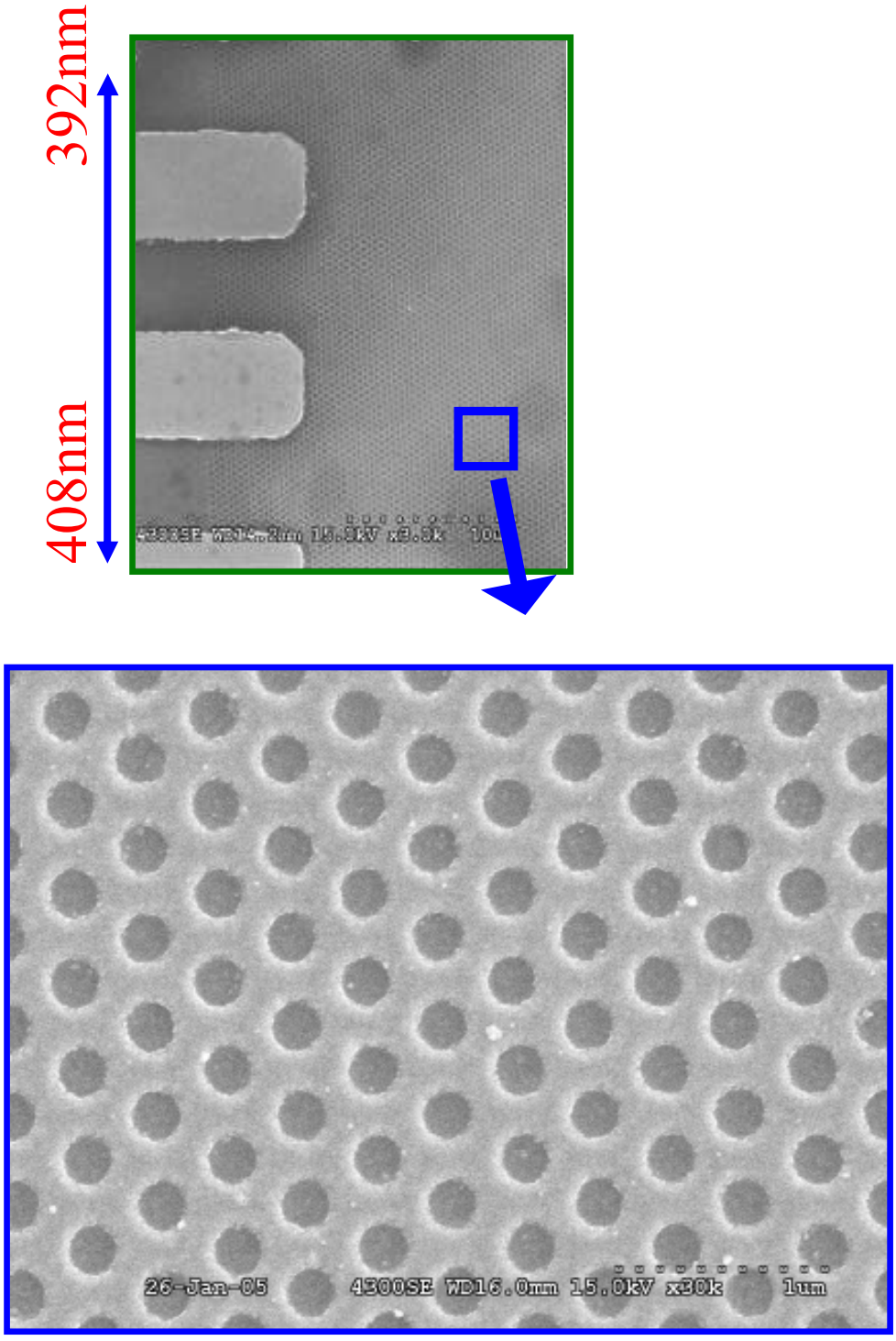


**Fig. 4-14 SEM micrograph shows the top view of the small gradient sample.**

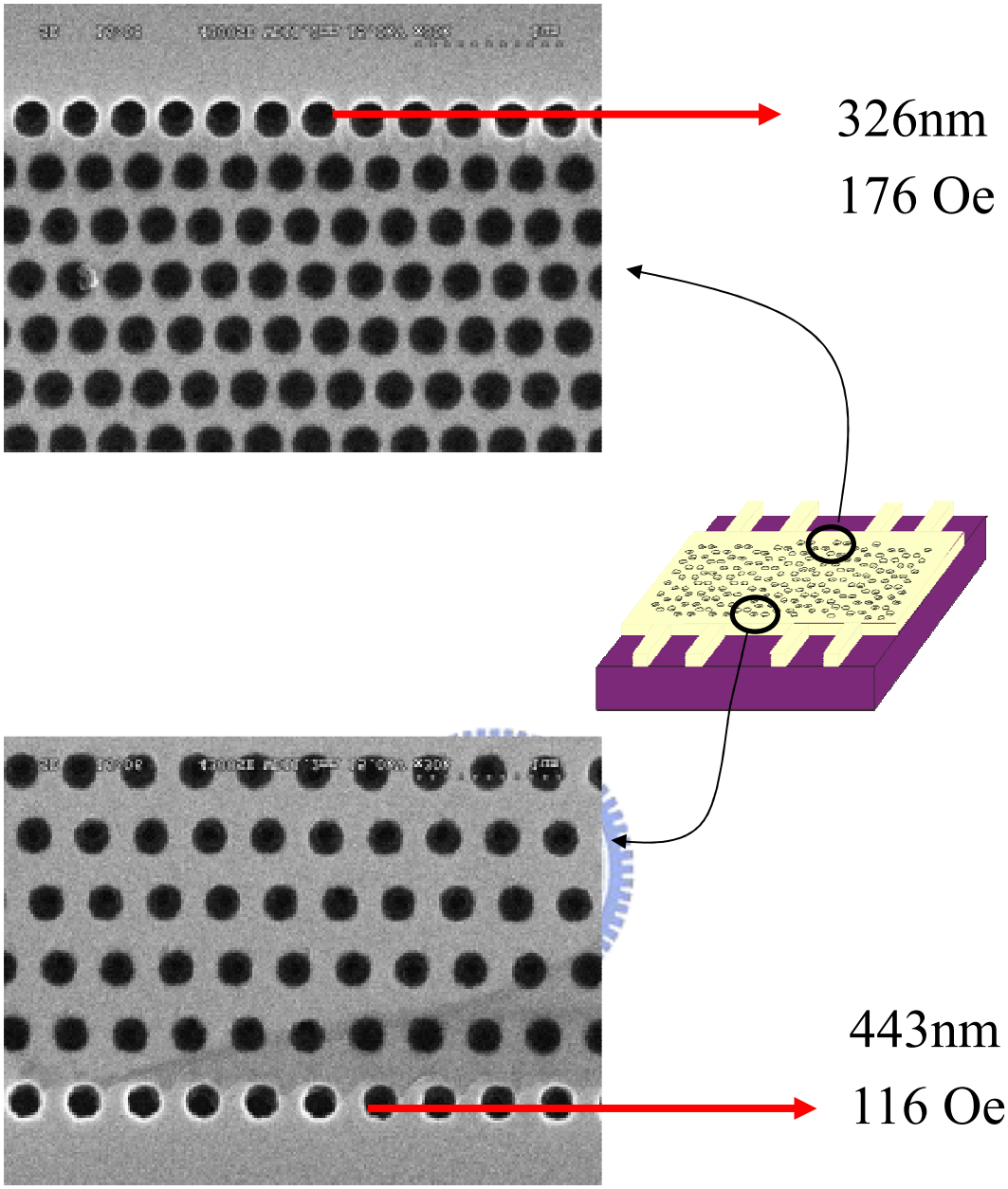


**Fig. 4-15 SEM micrograph shows the top view of the large gradient sample.**

## (1) Small gradient sample

The Magnetoresistance with respect to $H/H_1$ for sample with spacing-graded of pinning sites is shown in Figure 4-17. The pinning property of the array is achieved by comparing the MR curves for injected positive/negative current along the x-axis ($I=100\ \mu A$) at 8.25 K. It was observed that commensurability effects take place and periodic minima appear in the MR curves up to the forth order at equal field intervals. The equal field interval is related to the average number density of pinning sites in the spacing-graded array. Here, we can define $H_1$ =145 Oe as the first matching field, at which the density of the vortex is equal to the number density of the holes.

It is interesting that these curves for positive/negative current are almost the same with MR curve measured for the regular triangle lattice sample with lattice constant of 400 nm. The MR curves of the present sample and the regular triangular hole array exhibit the same background dissipation in between the integer matching fields and the same matching fields $H_n = nH_1$, but the reduction in dissipation are remarkably different around matching fields as shown in the right inset of figure 4-17. It appears that the asymmetry of pinning property with respect to current direction should be present at matching fields. One can clearly see that the resistance for the positive current is much higher than that for the negative current at matching fields. Note that the positive current corresponds to vortices move from high density region of pinning sites to low density region.

At H<0, one can observe a clear sign inversion of the dc voltage around the matching fields. All results are reversal at negative fields, which means the dc voltage drop for the negative current is much higher than that for the positive current. This indicated that the vortices easily move to the direction of low density of pinning sites.

Furthermore, the pronounced asymmetry of pinning properties of the sample can also be reached from the IV curves. We chose two constant applied fields, one is

first matching field (145 Oe) and the other is below the first matching field (120 Oe), as shown in Fig. 4-16. The IV curves can show a similar behavior comparable to MR curves. The voltage-current curves are essentially the same for field out of matching field, as shown in Fig. 4-16. However, there are significant differences in the IV curves for positive/negative injected current at first matching field. The dc voltage drop for the negative current is much lower than that for the positive current, as shown in Fig 4-16. Similar results are also found in other matching fields. This manifested that the vortices are strongly pinned at pinning sites for injected negative current and the difference of voltage drop comes from the symmetry breaking of spacing-graded array for injected positive/negative current.

Again all results are reversal at negative fields; one can observe a clear sign inversion of the dc voltage around the matching fields. The IV curve for the negative current is much higher than that for the positive current.

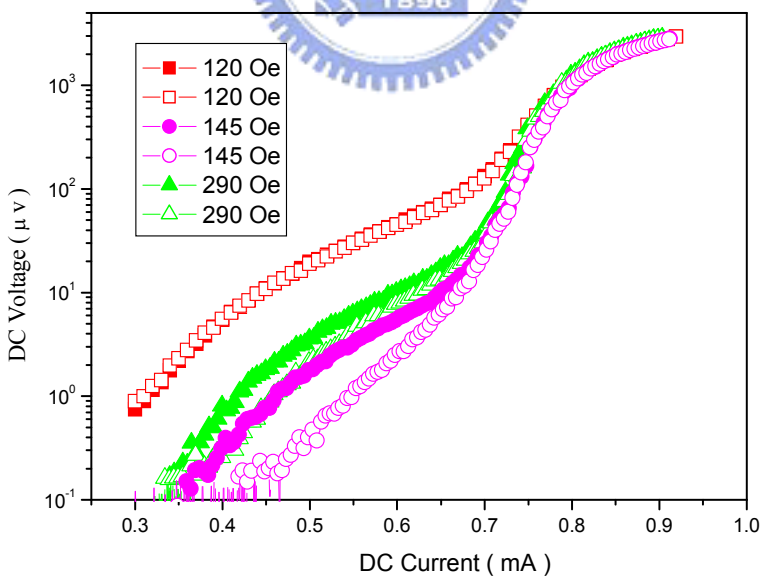


**Fig. 4-16 dc voltage vs dc applied current for a Nb film with graded pinning site's density at first matching field.**

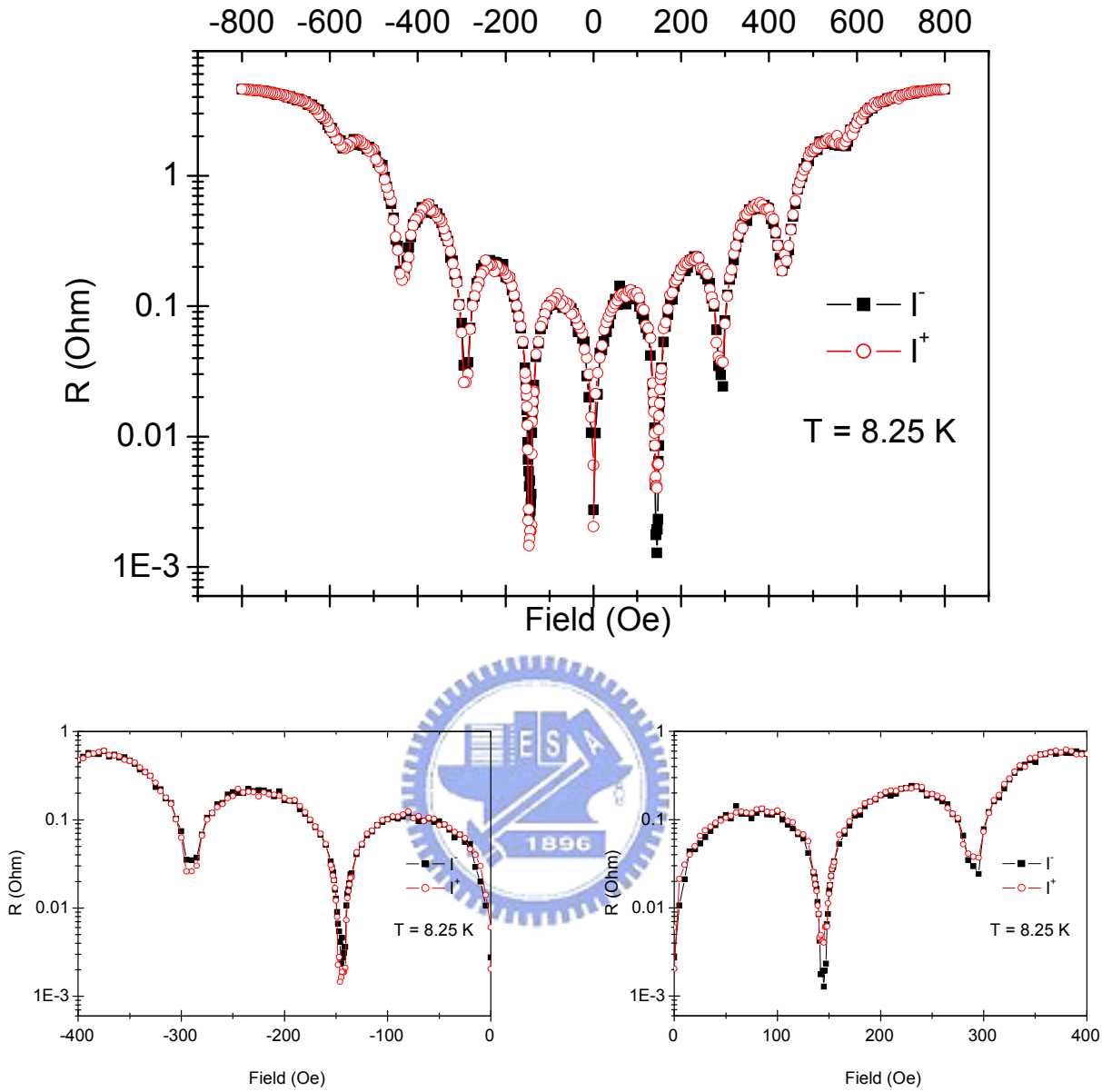


**Fig. 4-17 (a) MR curves for injected positive/negative current at T= 8.20 K. The inset (b) and (c) show sharp and shallow dips around the first matching field.**

## (2) Large gradient sample

MR curves measured at 7.90 K are plotted for several different current densities for applying current along x-axis, as shown in Fig. 4-18(a). The pinning properties for the graded array of pinning sites are less effective than those for regular ones because the vortices can not be stabilized in such a quasi-regular hole array. Periodic minima at matching fields are absent in the MR curves. Two kinds of MR curves can be found in Fig. 4-18(a). For injected high current, vortices are moving and the resistivity increases below the first matching field. There are little dips in the MR curves at H=68 Oe (I = 300 μA) and 124 Oe (I = 300 μA and 500 μA). The reduction in dissipation, however, is visible in a tiny range of temperature and for high injected current. It is noticed that the flux density at 124 Oe has a relation to the pinning density, that is, the lattice constant of the bottom row is 443 nm. When the magnetic field is increased, portion of the vortices seems to be locked into the bottom pinning row. However, at the magnetic field of 172 Oe which corresponds to the lattice constant of the top row (326 nm), a reduction of dissipation is not seen. Vortex lattice is more effectively pinned at low density of pinning sites than at high density of pinning sites.

For injected low current, MR curve shows a sharp onset of the resistivity for an applied magnetic field close to the first matching field, i.e. 150 Oe at 7.90 K, and the resistivity increases monotonic until normal state. The onset of the resistivity is also observed at matching fields in many MR curves for superconductor with regular periodic array of pinning sites for low temperature or low injected current on matching fields. Figure 4-18(b) shows a set of MR curves measured at lower temperature of 7.86 K with different current strengths. The curves show two separate groups where the sharp onsets of resistivity exhibit at field equal to 150 Oe and 300 Oe, respectively. The flux densities at those onset fields are related to the average

density of pinning sites, which is in agreement with lattice constant of 400 nm for regular array. This means pinning force is strong enough at low temperature to distort the vortex configuration which matches the quasi-regular pinning array. As the magnetic field is further increased above the matching fields, as soon as the interstitial vortices appear, the pinned vortices start to be pushed out of the hole array. The pinned vortices start to move and avalanches take place. Then the dissipation of resistivity shows a monotonic flux-flow behavior without any characteristic features.

## (3) Discussion

The geometric nature of the hole-array over which the vortex moving play a dominant role for vortex pinning at the matching fields. The pinning energy provides by the pinning site let the vortex persist in the pinning site. Vortices can be trapped on the pinning sites as soon as the vortices are penetrated into the Nb film. Then the pinned vortices produce a deformation in the vortex lattice. The commensurability effects, which were found in symmetry configurations of pinning array, should related to the interplay between pinning energy and vortex lattice deformations. Otherwise, the commensurability effect is absent in irregular configuration of pinning array. In our sample, the 4-th matching field was found in MR curves. It is important to note that as long as the variation of the hole spacing is small, the vortex lattice still forms regular orientation at matching fields on such a qusi-regular array of pinning sites. That's why the MR curve of the graded sample is the similar with right triangular lattice. But when the gradient of the hole spacing is large enough, such commensuration doesn't exist because the vortex lattice can not stabilize in such hole array. This implied that the vortex lattice is more strongly pinned at matching fields when the array is symmetric.

At matching fields, the graded density of the pinning site causes the graded

density of the trapped vortices. The pinning landscape at matching fields formed in the spacing-graded pinning sites has an asymmetry that is probed by the vortex lattice because the vortex-vortex interaction force increases from high concentration side to low concentration side. We relate the difference of the MR curves at matching fields to the vortex-vortex interaction force is present in our array. A net force may act on a single trapped vortex by the nearest trapped ones. The net force is in a direction opposite to flux density gradient. The graded pined vortices result in a ratchet that based on the change of the pinning threshold energy. The depinning force is suggested to be asymmetric. Thus, the reduction in dissipation should be change for different direction of external force, which means the vortex lattice slows down in different value. The total force acts on the vortex is large when the injected positive current makes the vortex flow fast. Thus, the overall resistivity minima values in negative currents were much lower than those in positive currents around matching fields.

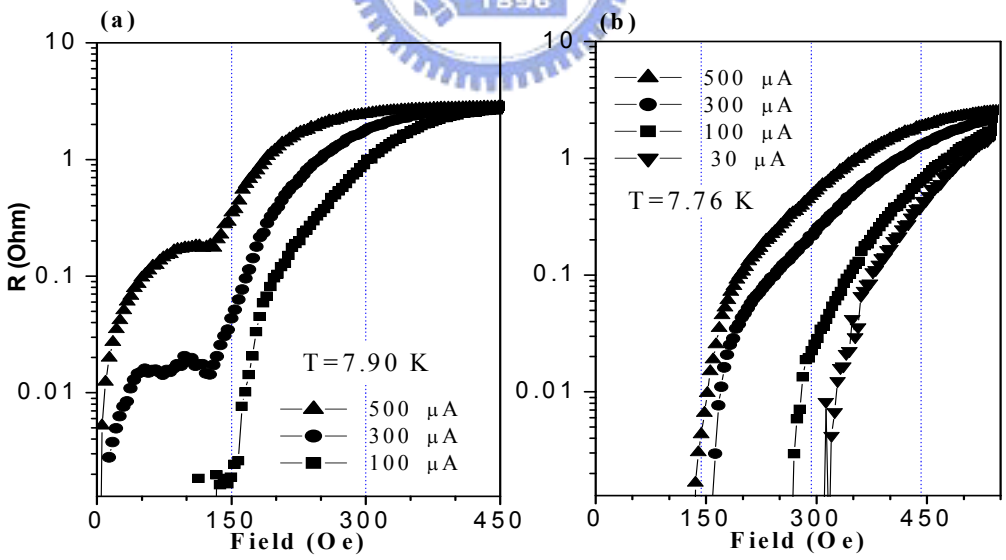


Fig. 4-18 **Magnetoresitance curves MR of a niobium film with spacing-graded array of holes in two opposite direction of dc current (negative current filled square, positive current open circle). (a) T = 7.90 K, (b) T = 7.86 K.**

## 4-4 Ratchet effect

Ratchet effect is being studied for guiding the motion of the particles when the Brownian motion of particles confine in asymmetric potentials. The concept of ratchet effect is referred to in mainly biological contexts (molecular motors [56] and molecular pumps [57]), vortex dynamics in superconductors [58-78] and many physical applications. These biological mechanisms can provide the proteins to do mechanical work or to transport ions, sugars etc in the living cells. In the case of vortex dynamics in superconductors, the influence of asymmetric potential has been opened up a new field and attracted interest.

The ratchet effect is obtained because of ac-driven vortices being rectified in asymmetric potential. The transport properties are carried out using an ac current

$$I=I_{ac}\sin(\omega t)$$

through the Nb superconducting film along the x-axis, where ω is an ac frequency (1kHz) and t is time. Thus the ac current density can give an ac Lorentz force acting on the vortices, that is given by

$$\vec{F}_l = \vec{j} \times \vec{n}\phi_0$$

(where $\vec{n}$ is a unitary vector parallel to the applied magnetic field), and the vortices are driven back and forth along the y axis. The time average of the AC Lorentz force, however, on the vortex is zero, that is

$$<F_L>=0.$$

According to the expression of the electron field

$$\vec{E} = \vec{B} \times \vec{v}$$

(with $\vec{B}$ the applied magnetic field and $\vec{v}$ the vortex velocity), we get that the dc voltage drop $V_{dc}$ measured along the direction of the injected current is proportional to the average velocity <v> of vortices in the direction of the ac driving force. The $V_{dc}$

recorded along the x-axis by a dc nanovoltmeter is

$$V_{dc} = \langle v \rangle dB$$

(where d is the distance between contacts and B the applied magnetic field). For the ac-driven vortices moving along the asymmetric sample, the output is a nonzero dc voltage $V_{dc}$. This means that a net vortex flow arises from the ac driving force, what shows that the sample induces a asymmetric potential landscape for the vortices. The magnitude of $V_{dc}$ depends on the amplitude of the ac current input $I_{ac}$. To further test this behavior, the ac current was injected along the long diagonal in the rhombic unit cell of the regular triangular array. In this case, the vortex lattice moves back and forth on this symmetric pinning potential and the output is a zero dc voltage.

Early work on the investigation of the vortex dynamics has been investigated in the mixed state of type II superconducting films with regular arrays of pinning sites [58-80]. The vortex dynamics on different shapes of pinning centers and arrays has been worked for instance by Schuller's group [59, 60] and Moshchalkov's group [61, 62]. Pinning effect has been extensively explored via magnetization [59, 62, 63], four-probe electric measurements [60, 61, 64] and theoretical simulations [65-68]. The commensurable effects demonstrate the attractive interaction between vortex and pinning sites, the repulsive interaction among vortices and result in complex behavior of vortex motion. In addition, matching effect appears when the vortex lattice matches the array of pinning sites. Recently to further get insight into the physics of vortex dynamics in superconductor, several schemes are proposed to investigate the rectification phenomena of the vortex lattice. Nori et al suggested several distinct ways of using potential energy ratchets and analyzed within the framework of the molecular dynamics (MD) simulations [71-72, 75].

Vicent et al. reported on reversible rectifier in Nb thin film with periodic array

of triangle pinning sites, which are asymmetric shape of pinning centers [73, 74]. It has been demonstrated that the interstitial vortex is balanced by inter-vortex repulsion. Vortices pinned on the pinning sites show a positive dc voltage. In addition, the interstitial vortices moved in opposite directions to that of the pinned vortices appeared a dc reversed voltage at a lower Lorentz force. Meanwhile, rectification effect in Al film with square array of asymmetric double-well pinning centers has been illustrated by the Moshchalkov et al [75-77]. The asymmetric pinning potential is characterized by the two critical depinning forces that come from two interpenetrating arrays of small and big pinning sites with small separation. The measurements revealed pronounce voltage rectification for a broad field range between 0 and 1.1 $H_1$, $H_1$ is the first matching field.

Instead of asymmetric pinning sites, a similar system has been realized in Nb films with semi-regular array of symmetry pinning centers in our research group. A spacing-graded array of submicrometer-scaled holes on the niobium thin films was first made by our group, and some results were presented in [78-80]. The arrays of hole are made asymmetry. From the Chapter 4-3, the magnetoresistance measurements and current-voltage characteristics reveal significant differences in the resistance value for positive/negative dc applied current at matching fields, while rectification voltage as a function of ac current $V_{dc}(I_{ac})$ shows well-defined nonzero sharp jump. These results demonstrated that the arrangement of the spacing-graded pinning center could strongly affect the rectification of the vortices. The behavior we found in our sample probably likes the results obtained from a lattice of asymmetric double-well pinning centers. The effect of asymmetric pin for our sample mainly comes from the action of vortex-vortex interaction. In addition, the long-range interactions are responsible for relative motions of vortex lattice. The graded pined vortices cause a net vortex-vortex-interaction force, thus local balance between net

vortex-vortex-interaction force and pinning force create a new equilibrium state. The depinning force is suggested to adjust the change of the pinning threshold energy for each direction.

As seen in preceding section, the geometry of the array can change the distribution of vortices and match the pinning array. The MR curves and IV curves reveal a competition between the elastic energy of the vortices and pinning energy at each pinning center. The arrangement of the pinning sites controls the distribution of the vortices. Vortex-vortex interaction changes the effective pinning landscape of vortices and asymmetric potential is formed. In this section, we will show the rectification effect in each sample which has different gradient. Two different amounts of gradient of the hole have been fabricated. The changing rates of smaller gradient sample and the larger one are 7.96% and 69.02%, respectively.

### 4-4-1 Small gradient array of pinning site

From Section 4-3 the asymmetric properties was shown in the transport measurement in the spacing-graded sample for positive/negative current, it is easy to find out the ratchet effect through the rectification of ac-driven vortices in our system. The results of the gradient sample can compare with the regular array. For the graded sample, the vortex lattice moves in this asymmetric pinning potential with a net velocity that results in nonzero dc response. This means that vortex lattice flows with a net velocity form the ac driving force and a ratchet effect occurs.

The rectification of ac-driven vortices as a function of ac applied current at integer and half-integer matching fields as shown in Fig. 4-19. The rectified voltage varies periodically with the number of vortices per pinning center. For all curves, the pronounced resonant rectification exhibits at matching fields and the $V_{dc}$ curves first increase steeply up to the maximum value and then decreases smoothly. The $V_{dc}$ at

matching fields become larger than the ones at intermediate magnetic fields. The rectified voltage shows broad and shallow curve in between the matching fields. This can be explained that the order vortex configuration formed at matching fields while the dynamics of the vortex lattice move coherently. In contrast, the $V_{dc}(I_{ac})$ curve for second matching field shows increasingly more pronounced. This clearly indicated that the weakly pinned interstitial vortices appear above the first matching field. The interstitial vortices were more strongly influenced by the applied current than pinned ones. At higher order matching field, however, the ratchet effect begins to decrease. The vortices block each other at high densities as vortex-vortex interaction increase. The $V_{dc}(I_{ac})$ curve at first matching field, however, exhibits different behavior than that at all the other matching fields. One sharp and one broad peak in the $V_{dc}$ curve are clearly seen, the $V_{dc}$ first increases steeply up to the maximum value and then decreases with an extra broad peak appearing in the $V_{dc}$ signal for the first matching field around 0.5 – 0.8 mA of ac current amplitude. Note that, the position of the broad peak coincides with the position of the peak in the difference of the two curves in Fig. 4-17, one is for dc current applied positive direction and the other is for the dc current applied negative direction for the first matching field. The IV curves for opposite injected currents shows difference only at matching fields. This infers that this asymmetric IV curve characteristics can be correlated with long-range order of vortex-vortex interactions of pinned vortices. We also had investigated the temperature dependence of broad peak [78]. The broad peak of $V_{dc}$ occurs at lower value of Iac and the magnitude of peak decreases for high temperature.

The rectified voltage as a function of ac applied current at first matching fields for different temperature are shown in Fig. 4-20. The thermal noise also affects the rectification. The whole peaks are shifted to low current density region with the increase of temperature. The jump of $V_{dc}$ occurs at lower value of $I_{ac}$ and the

magnitude of jump also decreases. Apparently, the net flow of vortices is developed when the vortex lattice is driven by ac current above the threshold of the critical current. The critical current is temperature dependent, because the thermal fluctuations are favorable for the depinning and melting of the vortex lattice. The sharp jumps in the rectified voltage become broader and shallower as the number of random vortices increase which is induced by thermal fluctuation. It is interesting that the broad peak is less pronounced while the temperature is increased. We can expect that the broad peak come from the pinned vortices sensing the asymmetric pinning energy. As the temperature is close to critical temperature, vortices can not easily be pinned on graded array of pinning sites. Thus, the appearance of a dc component of the voltage is no longer contribution to the $V_{dc}(I_{ac})$ curve and absent at high temperature.

The sharp jump in the rectified voltage curve is the predominant feature in the Vdc(Iac) curve and also visible for other fields. In addition, sharp dips change with applied magnetic field and the Vdc(Iac) curves can be found more complicated depending on the number of the moving vortices which is increased by the applied magnetic fields below first matching field. We found another interesting effect in our samples for applied magnetic field just below the first matching field. Take the curve at 120 Oe for example, a dc-reversed signal was observed. The result of such an experiment can be seen in Fig. 4-21(H). A more detailed description of the change of the sharp jump in the $V_{dc}(I_{ac})$ curves for different applied field, the maximum rectification value ($V_{max}$) of the sharp jump was extracted from the $V_{dc}(I_{ac})$ curves, as shown in Fig. 4-22 which is as a function of applied magnetic field. The $V_{max}(H)$ profile showed a peak at first matching fields and changed drastically in the vicinity of the first matching field. With the increase of the magnetic field, this positive dc voltage enhanced gradually until H=40 Oe. Then above 40 Oe the rectified values

were progressing diminished. It is noticed that a dc-reversed signal began to develop in the range of 100 - 138 Oe. The negative voltage decreases with further increase magnetic field. Then, rectified voltage reversed abrupt in the vicinity of first matching field and had maximum value at the first matching field.

The observed matching effects for sample with spacing-graded array of pinning sites suggest that the slight displacement of the holes may not destroy the symmetry of the array. The elastic vortex lattice can show plastic flow and moving crystal phase when vortex lattice interacts with spacing-graded pinning array. The plastic flows which are subject to random pinning begin at the onset of depinning when portions of the vortices become mobile while other portions remain pinned. These phases of flows can be inferred experimentally via the dc voltage produced by the moving vortices. Vortex lattice first flows plastically and then undergoes a dynamic transition from a disordered structure to an ordered moving vortex lattice when vortex lattice matches the underlying pinning sites. It is clear that the coherence moving vortices are intense under the domination of pinning array. Therefore, the periodicity of the minima appears in the magnetoresistance and vortex lattice locks into the hole array (see Fig. 4-16 also see Fig. 4-23), while the ac-driven vortex lattice induces coherent vortex motion and enlarges rectified voltage for matching field (see Fig. 4-20).

The maximum rectified value ($V_{max}$) of the sharp jump shows quantitative change with respect to the magnetic field, as shown in Fig. 4-22. We relate the phase change to the competition between the plastic dynamics of the vortices and coherent vortex motion. The result disclosed significant related to the MR curve in figure 4-23. From the result of figure 4-23, the dissipation of MR curve at matching fields indicated the dynamic ordering of the vortex lattice. To make a comparison between these two charts, three different kinds of slop can be clearly recognized below the first

matching field in the MR curve of Fig. 4-23. When $dR/dH >> 0$, dc voltage is positive; whereas $dR/dH << 0$, dc voltage is negative.

The driven vortices start to form plastic flows by injected current. The vortices move on the spacing-graded potential that belongs to irregular or asymmetric potential, thus the ratchet effect may be observed in the spacing-graded sample. The positive dc voltage enhanced gradually until H=40 Oe in the regime of $dR/dH >> 0$, reflecting the ratchet effect became important while the magnetic field is increased. One possible reason of the increase of the $V_{max}$ value is that more and more vortices penetrate to the film and are getting involved with the rectification. Then above 40 Oe the rectified values were progressing diminished since the vortex-vortex interaction became more relevant. It is reasonable to assume that higher vortex density causes stronger vortex-vortex repulsion that hampers the moving channels of the plastic flow vortices and tends to decrease the dc vortex response, while the MR curve become gentle as a result of random moving of the vortices. The magnitude of the rectified vortex flow further decreases monotonously as vortex density increased. Then a dc-reversed signal began to develop and the negative voltage decreases with the increase of the magnetic field in the regime of $dR/dH << 0$. The large amount of vortices can hamper their own relative motions. As a result of a mutual vortex interaction, the individual vortices transform into an order vortex lattice on the array of pinning site, this is, the vortex lattice stare to locks into the pining sites. Then the vortices undergo elastic flow besides plastic flow. In addition, the number of the vacant pinning sites decreased when the number of vortices increased. Hence, it is possible to form a number of vacancies in the vortex lattice. The dynamical properties of vacancies may be different from that of the vortices. This situation is similar to

electrons and holes in semiconductors. Thus the ratchet effect it produces to be reversed. Around the matching field, the pinning effect caused by holes is most effective when the vortices are arranged regularly and stably. The long range order of the vortex lattice develops a dynamic ordering system. Once again, we may see the asymmetry of ratchet effect reversed abrupt in the vicinity of first matching field. As we can see in Fig. 4-21(K) also in Fig. 4-22, plastic flow and moving crystal phase give rise to two ratchets at first matching field. It is interesting that the same results also got from the superconducting film with double-well pinning centers by V. V. Moshchalkov et al. [75-77]. Their explanation for this double ratchets was that the interplay between the incommensurate vortex rows and the whole vortex lattice. In our case, the spacing-graded array of hole cause asymmetric property and keep original symmetric property of regular array.

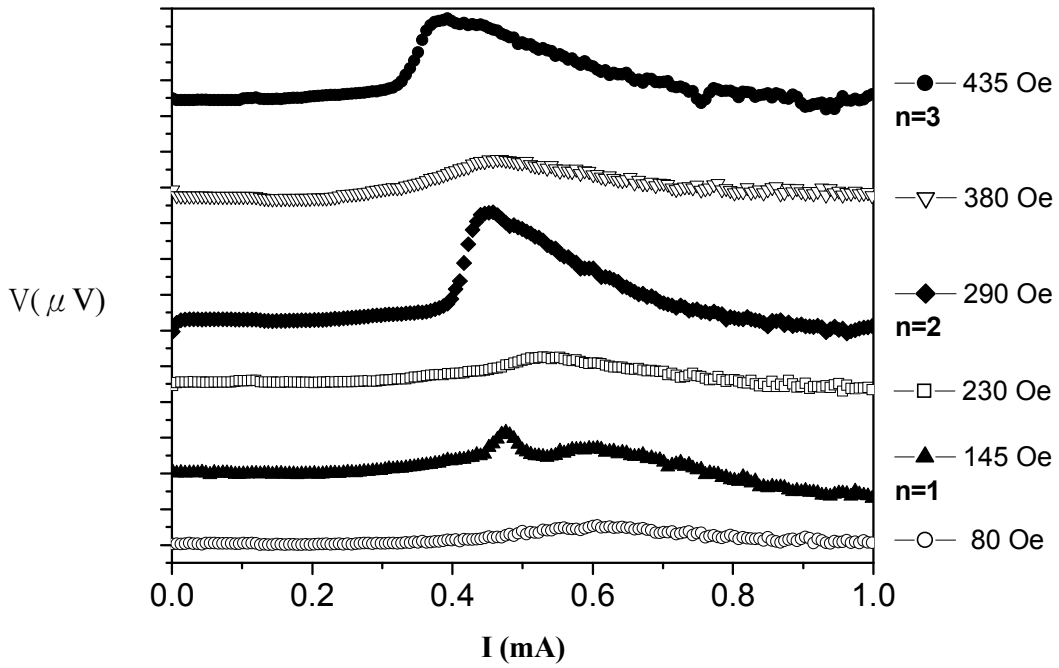


Fig. 4-19 Dc voltage drop $V_{dc}$ as a function of ac current $I_{ac}$ for different applied magnetic fields.

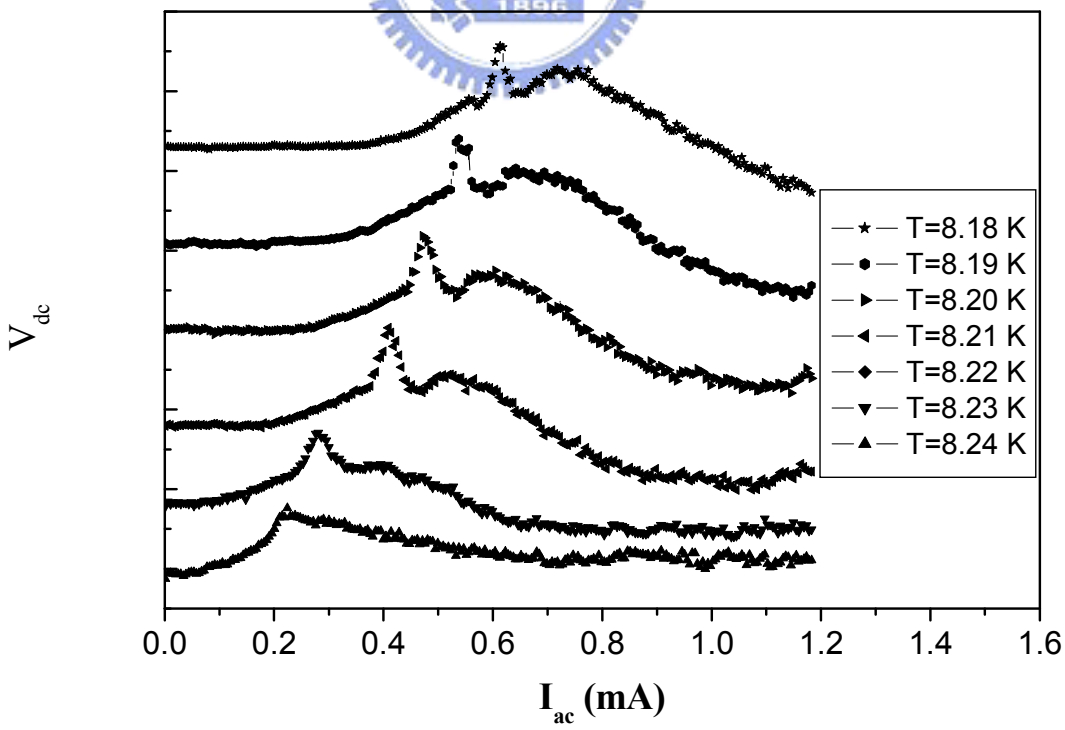


Fig. 4-20 Dc voltage drop as a function of ac current for different temperature.

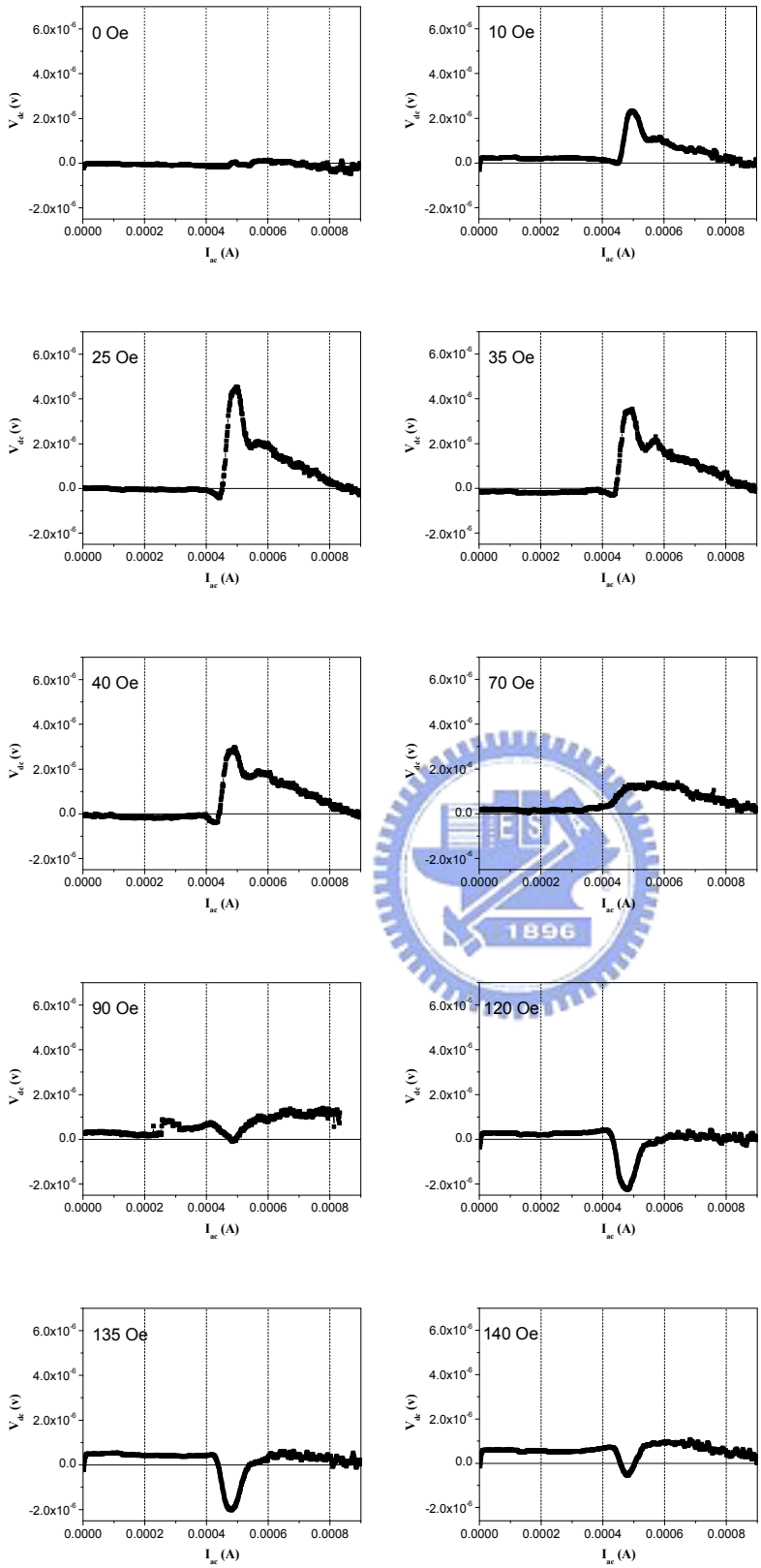


Fig. 4-21 The $V_{dc}(I_{ac})$ for different applied magnetic field at T = 8.20 K.

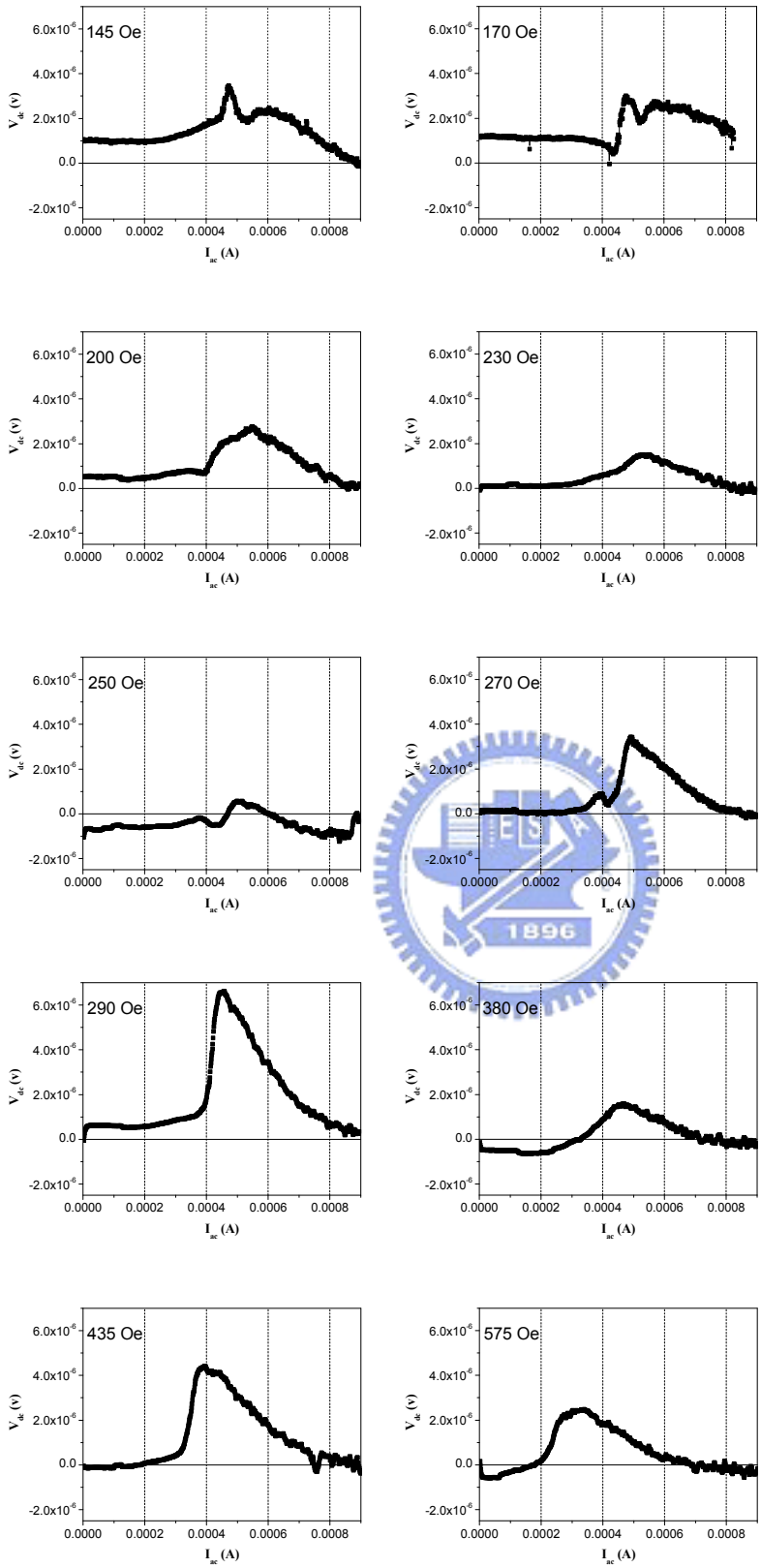


Fig. 4-21 The $V_{dc}(I_{ac})$ for different applied magnetic field at T = 8.20 K.

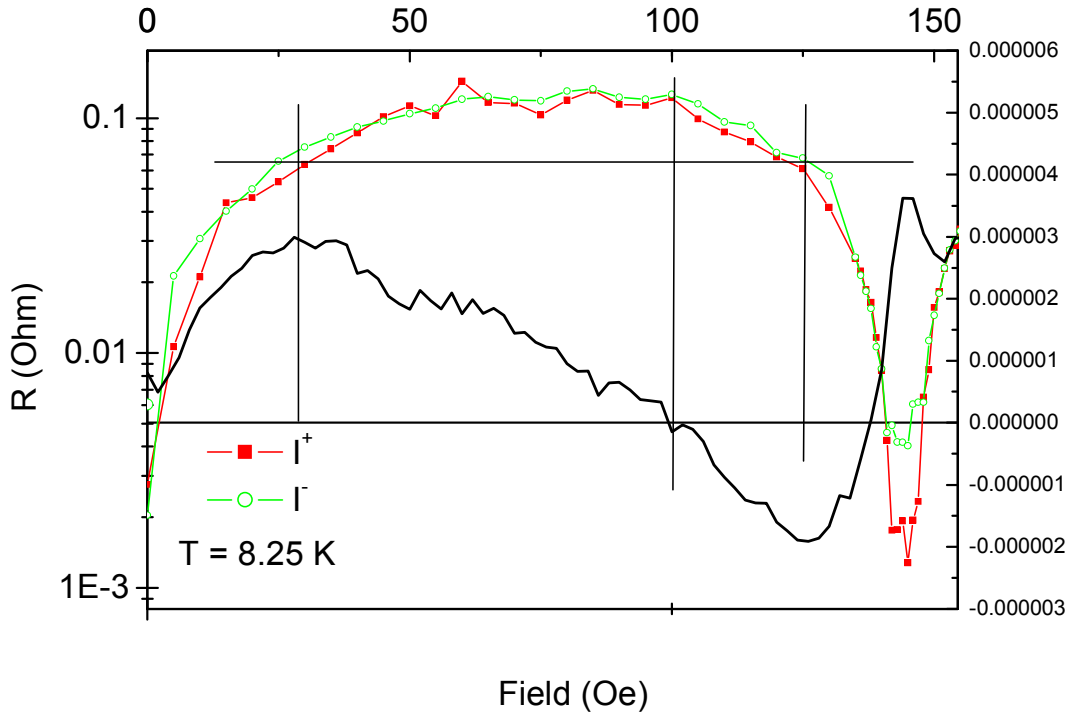


Fig. 4-22 The comparison between the maximum rectified value ($V_{max}$) and Magnetoresistance as a function of applied magnetic field.

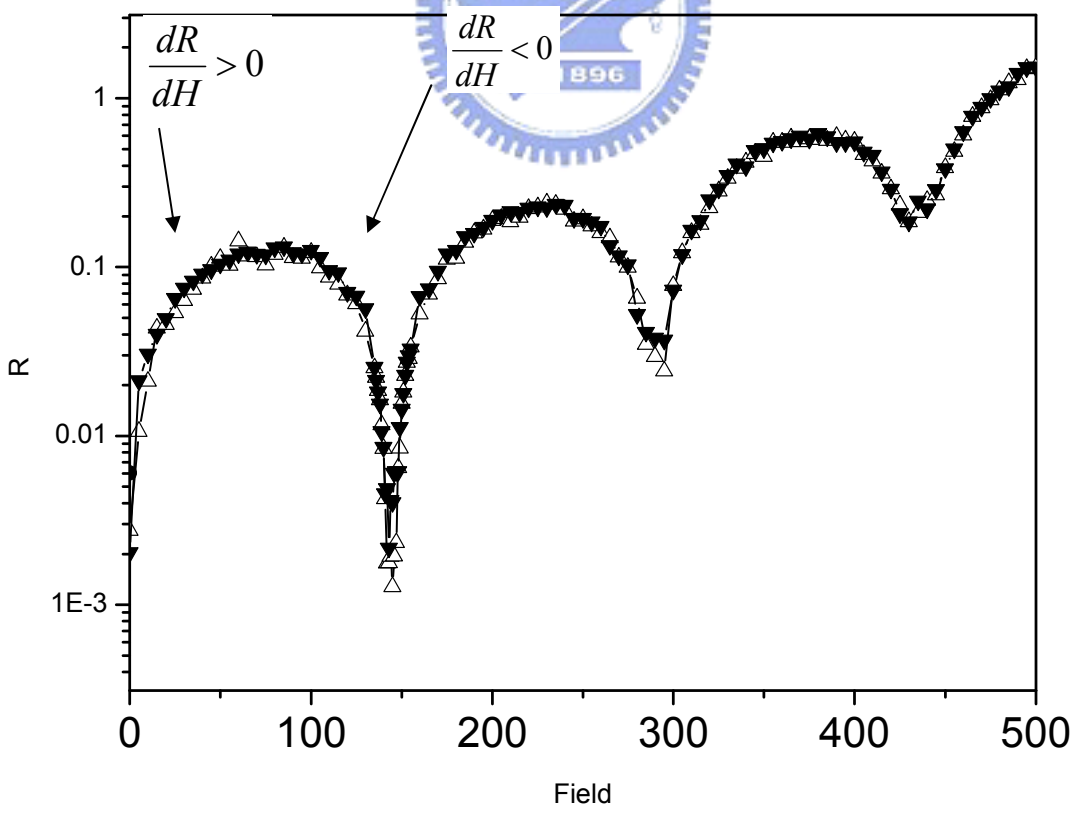


Fig. 4-23 Magnetoresistance as a function of applied magnetic field.

### 4-4-1 Large gradient array of pinning site

Figure 4-24 clearly shows a nonzero dc voltage $V_{dc}$. It should be noted that the dc voltage as a function of ac current shows an important feature of the ratchet effect at a fixed applied field. This means that a net vortex flow toward y direction arises. The dc voltage strongly depends on the amplitude of the applied ac current.

By comparing the results obtained for our sample, we notice the markedly difference in the rectified voltage below and above the first matching field. Figure 4-24 (a)-(f) show the rectified voltage for several selected magnetic fields. Basically, the $V_{dc}$ increases monotonically up to a maximum value and then decrease smoothly. The positive-rectified voltage corresponds to the motion of vortices from a region of high density pinning sites to a low density region. As the magnetic field is increased, the maximum rectified voltage ($V_{max}$) increased until a field H = 150 Oe, as shown in Fig. 4-24(c). In addition, the curves shift toward low current density value as magnetic field increase below the first matching field. Another important effect shown in Fig. 4-24(a) and Fig. 4-24(b) is that two types of ratchet phases labeled as I and II are being observed below the first matching field. It should be noted that the amount of pinning sites is larger than that of the vortices. In Phase I, a portion of vortices which are near the vacant pinning sites first rectified by the ac injected current. In Phase II, the whole vortex lattice is being rectified. With the number of the empty pinning sites decreased, Phase I disappears near the first matching field. The rectified voltage abruptly increases and presents a maximum enhancement in the rectification at the first matching field. For magnetic field above first matching field, the maximum rectified voltage starts to drop and a negative voltage forms in the rectified curve, as shown in Fig. 4-24 (d)-(f).

As can be seen in Fig. 4-24 (c), the first matching field is the borderline of two different vortex motions. To emphasize the borderline at first matching field, the

maximum in the rectification ($V_{max}$) is depicted as a function of the applied field, as shown in Fig. 4-25 (a). The rectification peak at the first matching field is the largest. The increase of the $V_{max}$ is due to that more and more vortices penetrate into the film and are getting involved with the rectification with the increase of magnetic field. When the maxima number of pinned vortices is rectified, the value of $V_{max}$ is largest. All vortices trapped at the pinning sites may collectedly contribute to the rectified voltage. Above the first matching field, the interstitial vortices appear and are rectified. The interstitial vortices do not directly interact with pinning sites; however, they are repelled by vortices trapped at the pinning sites. The interstitial vortices were rectified in the opposite direction to the pinned vortices. The reversal drift of the interstitial vortices leads to a negative signal at low drives. Similar results are also reported by Nori in Ref. [81, 82]. The rectified value of the interstitial vortices increased with increased applied field, as shown in filled-square curve of Fig. 4-25 (a). The interstitial vortices would block the motion of the pinned vortices, thus the rectified voltage of pinned vortices begins to decrease at high applied magnetic field.

It is interesting that the position of the peak ($I_{max}$), the ac current at which the dc voltage is maximum, decreased with increasing applied field until the first matching field. Then maximum rectified voltage decreased and $I_{max}$ keeps constant at the same current around 350 μA. Meanwhile the value of the negative rectified voltage increased and the position of the dip keeps constant at the same current around 150 μA for every curve above the first matching field. These trends are illustrated in Fig. 4-25 (b). The position of peaks strongly depends on the magnetic field amplitude below the first matching field. It should be noted that the vortex-vortex interaction plays an important role in this situation. The vortex-vortex interaction force is larger for vortices in high concentration side than in low concentration side. Thus the effective pinning potential is small for vortices in high

concentration side, and vortices prefer to locate at pinning sites in low concentration region. The increasement of the vortex-vortex interaction causes the vortices being pushed out of pinning sites easily. The average effective pinning potential would decline with the increase of the vortex density, so $I_{max}$ decreases towards lower value as magnetic field increases until the density of pinning sites are equal to the density of vortices.

The position of the positive/negative rectified voltage, however, is located at the same applied current equal 350 μA (open symbols in Fig. 4-25 (b))/150 μA (filled symbols) for magnetic field above the first matching field. The interstitial vortices are confined between the pinned vortices and balance by the pinned vortices. Thus, the interstitial vortices were more easily influenced by the applied current than the pinned vortices. The constant current of 350 μA indicated that every pinning center that catches a vortex will hold onto it up to a certain maximum pinning force and depins at certain applied current.

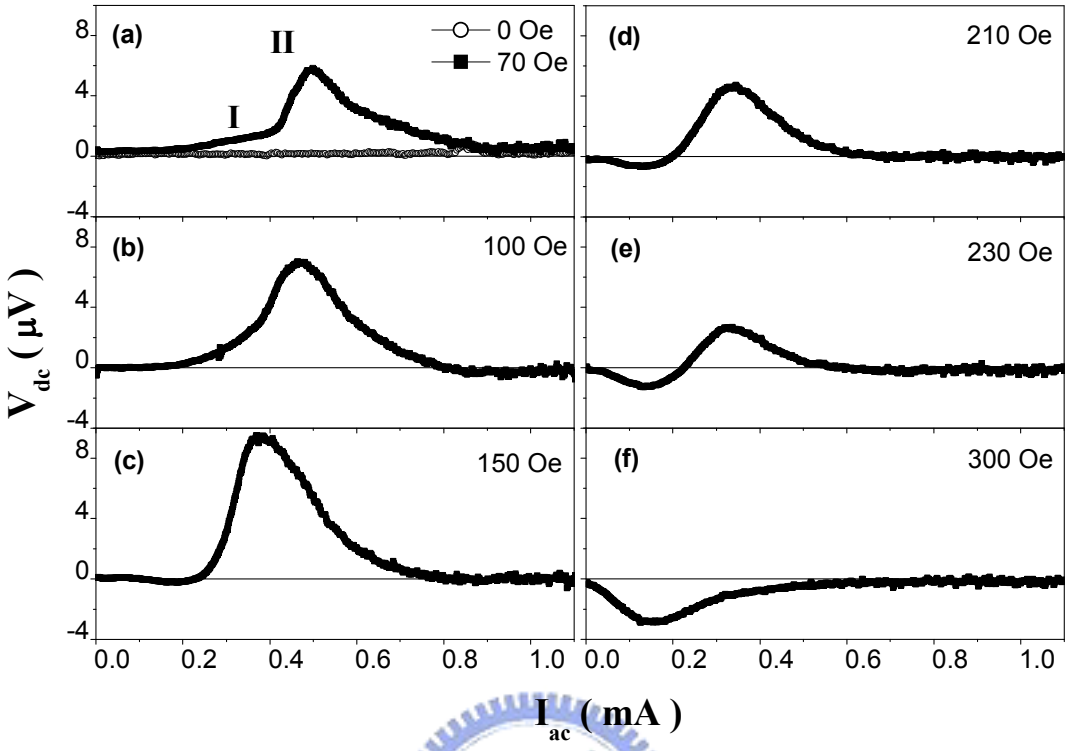


**Fig. 4-24** Dc voltage drop $V_{dc}$ as a function of ac current $I_{ac}$ for different magnetic field. Panels (a)-(b): $H<H_1$. Panel (c): $H=H_1$. Panel (d)-(f): $H>H_1$. $H_1$ is the first matching field and is equal to 150 Oe.

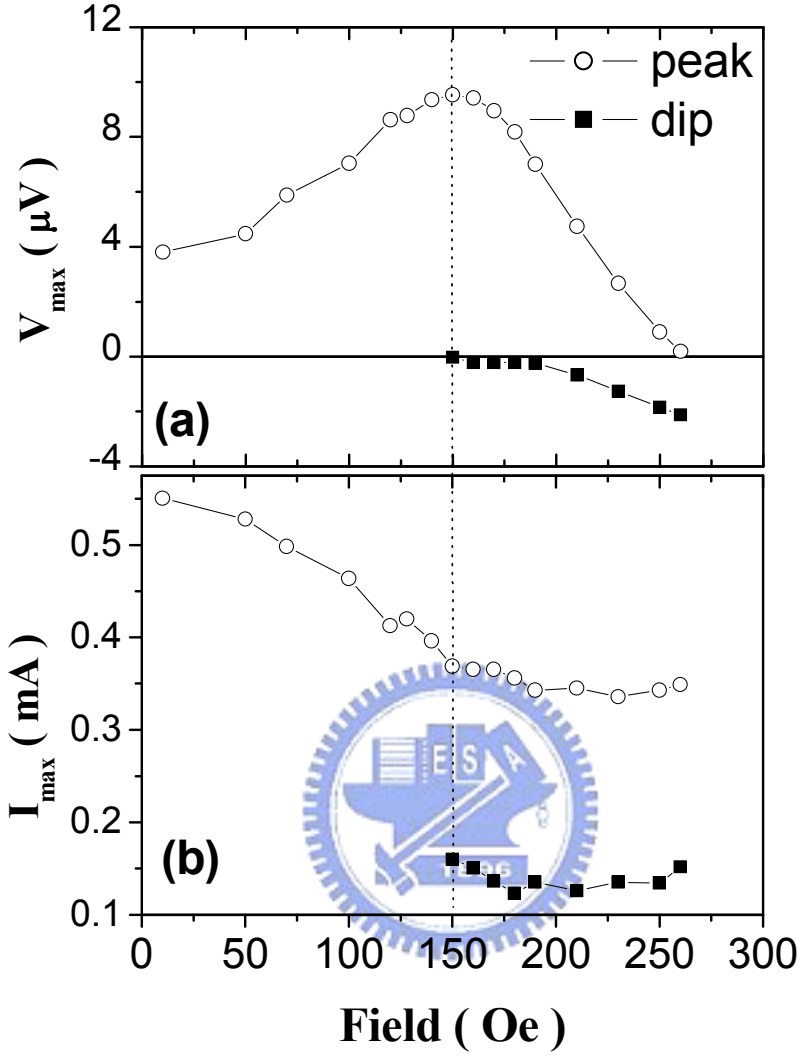


**Fig. 4-25** (a) The dependence of the maximum/minimum rectification dc voltage ($V_{max}$) in the $V_{dc}(I_{ac})$ curves of the peak/dip for different applied magnetic field. (b) the position of peak (open symbols) and dip (filled symbols) as a function of applied magnetic field.

# Chapter 4

# Conclusion

The transport of vortices has been investigated in Nb superconductors with spacing-graded arrays of submicrometer-scaled holes in this thesis. The Nb superconductors with spacing-graded density of holes, subject to a magnetic field perpendicular to the film plane, exhibit rectification effect when the vortex lattice is driven by ac current. The superconducting films work as rectifiers, which can generate a dc electric field along the direction of the ac current, due to unavoidable vortex pinning. Two samples with different gradient rate of the hole were studied in this work. The asymmetric geometry of the pinning array produces a significant influence on the vortex motion. The rectified voltage depends considerably on the amplitude of the applied ac current and the magnetic field. In addition, the rectified voltage depends strongly on the temperature.

For small gradient sample, the arrangement of the hole array is nearly similar to the regular triangular array. The magnetoresistance shows several dips at matching field for the number of vortices per unit cell. The magnetoresistance measurements and current-voltage characteristics reveal significant differences in the resistance value for positive/negative dc applied current only at matching fields. In the superconducting films with spacing-graded array of holes the rectified voltage varies periodically with the number of vortex per pinning center.

For large gradient sample, the arrangement of the hole array is totally different to the regular triangular array. The magnetoresistance shows no dip at matching field. The experimental results reveal that a drastic change of the vortex rectification for

magnetic field above/below the first matching field. The reason may be that the interstitial vortices are formed in the film above the first matching field. A reversible vortex motion is induced by the interstitial vortices for the field above the first matching field.

Anisotropic pinning effects are dominant contribution to the rectification. The arrangement of the pinning sites controls the distribution of the vortices. Vortex-vortex interaction changes the effective pinning landscape of vortices and asymmetric potential is formed. The ratchet effect of vortices is created on spacing-graded array of pinning landscape.

## Reference


1. M. Tinkham, Introduction to Superconductivity (McGraw-Hill. New York, 1975).

2. G. Blatter, M. V. Feigel'man, V. B. Geshkenbein, A. I. Larkin, and V. M. Vinkur, Rev. Mod. Phys. 66, 1125 (1994).

3. A. E. Koshelev and V. M. Vinokur, Phys. Rev. Lett. 73, 3580 (1994).

4. T. Gianmarchi and P. Le Doussal, Phys. Rev. Lett. 76, 3408 (1996).

5. Hans Hilgenkamp, Victor V. Moshchalkov, and Peter Kes, Science 302, 1159 (2003).

6. F. Nori, Science 271, 1373 (1996).

7. O. Daldini, P. Martinoli, J. L. Olsen, and G. Berner, Phys. Rev. Lett. 32, 218 (1994).

8. A.T. Fiory, A. F. Hebard, and Somekh, Appl. Phys. Lett. 32, 73 (1978).

9. P. Selders, A. Castellanos, M. Vaupel, and R. Wördenweber, Appl. Supercond. 5, 265 (1997).

10. J. F. Schmyth, S. Schultz, D. R. Fredkin, D. P. Kern, S.A. Rishton, H. Schmid, M. Cali, and T. R. Koehler, J. Appl. Phys. 69, 5262 (1991).

11. A. Maeda, M. Kume, T. Ogura, K. Kuroki, T. Yamada, M. Nishikawa, and Y. Harada, J. Appl. Phys. 76, 6667 (1994).

12. K. J. Kirk, J. N. Chapman, and C. D. W. Wilkinson, Appl. Phys. Lett. 71, 539 (1997).

13. Win Vinckx, Johan Vanacken and Victor V. Moshchalkov, J. Appl. Phys. 100, 044307 (2006).

14. M. Kemmler, C. Gurlich, A. Sterck, H. Pohler, M. Neuhaus, M. Siegel, R. Kleiner and D. Koelle, Phys. Rev. Lett. 97, 147003 (2006).

15. Jose I. Martin, M. Velez, A. Hoffmann, Ivan K. Schuller, and J. L. Vicent, Phys. Rev. Lett. 83, 1022 (1999).

16. U. Welp, Z. L. Xiao, J. S. Jiang, V. K. Vlasko-Vlasov, S. D. Bader, G. W. Crabtree, J. Liang, H. Chik, and J. M. Xu, Phys. Rev. B 66, 212507 (2002).

17. A. V. Sihanek, W. Gillijns, V. V. Moshchalkov, B. Y. Zhu, J. Moonens and L. H. A. Leunissen, Appl. Phys. Lett. 89, 152507 (2006).

18. Charles Reichhardt and Niels Gronbech-Jensen, Phys. Rev. Lett. 85, 2372 (2000).

19. C. Reichhardt, C. J. Olson and Franco Nori, Phys. Rev. B 58, 6534 (1998).

20. G. R. Berdiyorov, M. V. Milošević, and F. M. Peeters, Phys. Rev. B 74, 174512 (2006).

21. K. Harada, T. Matsuda, J. E. Bonevich, T. Yoshida, U. Kawabe, A. Tonomura, Nature 360, 51(1992).

22. C. Reichhardt, C. J. Olsen, and Nori, Phys. Rev. B 57, 7937 (1998).

23. G. S. Mkrtchyan and V. V. Shmidt, Sov. Phys. JETP 34, 195 (1972).

24. A. Bezryadin and B. Pannetier, J. Low. Temp. Phys. 102, 73 (1996).

25. A. Hoffmann, P. Prieto, and I. K. Schuller, Phys. Rev. B 61, 6958 (2000).

26. Charles Reichhardt and Niels Gronbech-Jensen, Phys. Rev. Lett. 85, 2372 (2000).

27. E. H. Brandt, J. Low Temperature Physics, 53, 41 (1983).

28. C.-S. Lee, B. Janko, I. Derenyi and A.-L. Barabasi, Nature 400, 337 (1999).

29. B. Y. Zhu, F. Marchesoni, V. V. Moshchalkov, and Franco Nori, Phys. Rev. B 68, 014514 (2003).

30. J. F. Wambaugh, C. Reichhardt, C. J. Olson, F. Marchesoni, and Franco Nori, Phys. Rev. Lett. 83, 5106 (1999).

31. H. Weinstock, Applications of superconductivity, Kluwer, Dordrecht, 1999.

32. H. Weinstock, SQUID Sensors, Kluwer, 1996.

33. M. B. Hastings, C. J. Olson Reichhardt, andC. Reichhardt, Phys. Rev. Lett. 90, 247004 (2003).

34. Arira Tonomura, Nature Materials 5, 257 (2006).

35. J. E. Villegas, Sergey Savelev, Franco Nori, E. M. Gonzalez, J. V. Anguita, R. Garca, J. L. Vicent, Science 302, 1188 (2003).

36. J. Van de Vondel, C. C. de Souza Silva, B. Y. Zhu, M. Morelle, and V. V. Moshchalkov, Phys. Rev. Lett. 94, 057003 (2005).

37. T. C. Wu, Master thesis (National Changhua University of Education, 2001).

38. Lance Horng, J. C. Wu, T. C. Wu, and S. F. Lee, Jour. Appl. Phys. 91, 8510 (2002).

39. Gerd Teniers, Martin Lange, Victor V. Moshchalkov, Physica C 369, 268 (2002).

40. M. J. Van Bael, J. Vekaert, K. Temst, L. Van Look, V. V. Moshchalkov, Y. Bruynseraede, G. D. Howells, A. N. Grigorenko, S. J. Bending and G. Borghs, Phys. Rev. Lett. 86, 155 (2001).

41. L. Van Look, M. J. Van Bael, K. Temst, J. G.. Rodrigo, M. Morelle, V. V. Moshchalkov, and Y. Bruynseraede, Physica C 332, 356 (2000).

42. M. J. Van Bael, K. Temst, V. V. Moshchalkov, and Y. Bruynseraede, Phys. Rev. B 59, 14674 (1999).

43. D. J. Morgan and J. B. Ketterson Phys. Rev. Lett. 80, 3614 (1998).

44. C. Peroz, C. Villard, A. Sulpice, and P. Butaud, Physica C 369, 222 (2002).

45. J. I. Martin, M. Velez, J. Nogues, and Ivan K. Schuller, Phys. Rev. Lett. 79, 1929 (1997).

46. Y. Jaccard, J. I. Martin, M.-C. Cyrille, M. Velez, J. L. Vincent, and Ivan K. Schuller, Phys. Rev. B 58, 8232 (1998).

47. M. J. Van Bael, M. Lange, S. Raedts, V. V. Moshchalkov, A. N. Grigorenko and S. J. Bending, Phys. Rev. B 68, 014509 (2003).

48. Q. H. Chen, G. Teniers, B. B. Jin, and V. V. Moshchalkov, Phys. Rev. B 73, 014506 (2006).

49. E. T. Filby, A. A. Zhukov, P. A. De Groot, M. A. Ghanem, P. N. Bartlett, and V. V. Metlushko, Appl. Phys. Lett. 89, 092503 (2006).

50. P. H. Lin, Master thesis (National Changhua University of Education, 2002).

51. P. C. Kang, Master thesis (National Changhua University of Education, 2003).

52. J. C. Wang, Master thesis (National Changhua University of Education, 2004).

53. C. W. Hsiao, Master thesis (National Changhua University of Education, 2006).

54. T. C. Wu, J. C. Wang, Lance Horng, J. C. Wu, and T. J. Yang, J. Appl. Phys. 97, 10B102 (2005).

55. R. Cao, T.C. Wu, P.C. Kang, J.C. Wu, T.J. Yang, and Lance Horng, Solid State Comm. 143, 171 (2007).

56. J. Howard, Nature 389, 561 (1997).

57. Philip J. Thomas and John F. Hunt, Nature Structural Biology 8, 920 (2001).

58. D. J. Morgan and J. B. Ketterson, Phys. Rev. Lett. 80, 3614 (1998).

59. A. Hoffmann, P. Prieto and Ivan K. Schuller, Phys. Rev. B 61, 6958 (2000).

60. M. Velez, D. Jaque, J. I. Martín, M. I. Montero, Ivan K. Schuller, and J. L. Vicent, Phys. Rev. B 65, 104511(2002).

61. L. Van Look, B.Y. Zhu, R. Jonckheere, B. R. Zhao, Z. X. Zhao, and V. V.

Moshchalkov, Phys. Rev. B 66, 214511 (2002).

62. E. Rosseel, M. J. Van Bael, M. Baert, R. Jonckheere, V. V. Moshchalkov, and Y. Bruynseraede, Phys. Rev. B 53, 2983 (1996).

63. U. Welp, Z. L. Xiao, J. S. Jiang, V. K. Vlasko-Vlasov, S. D. Bader, G. W. Crabtree, J. Liang, H. Chik, and J. M. Xu, Phys. Rev. B 66, 212507 (2002).

64. T. C. Wu, P. C. Kang, L. Horng, J. C. Wu, and T. J. Yang, J. Appl. Phys. 95, 6696 (2004).

65. C. J. Olson, C. Reichhardt, Franco Nori, Phys. Rev. Lett. 81, 3757 (1998).

66. Charles. Reichhardt and Niels Gronbech-Jensen, Phys. Rev. B 63, 54510 (2001)

67. M. V. Milosevic, and F. M. Peeters, Phys. Rev. Lett. 93, 267006 (2004).

68. G. R. Berdjyorov, M. V. Milosevic, and F. M. Peeters, Phys. Rev. Lett. 96, 207001 (2006).

69. A. V. Silhanek, L.Van Look , R. Jonckheere, B. Y. Zhu, S. Raedts, and V. V. Moshchalkov, Phys. Rev. B 72, 014507 (2005).

70. Veronica I. Marconi, Physica C 437, 195 (2006).

71. B. Y. Zhu, F. Marchesoni, and Franco Nori, Physica E 18, 318 (2003).

72. J.F. Wambaugh, C. Reichhardt, C. J. Olson, F. Marchesoni, and Franco Nori, Phys. Rev. Lett. 83, 5106 (1999).

73. J. E. Villegas, Sergey Savel'ev, Franco Nori, E. M. González, J. V. Anguita, R.

Garcia and J. L. Vicent, science, 302, 1188 (2003).

74. J. E. Villegas, E. M. Gonzalez, M. P. Gonzalez, J. V. Anguita, and J. L. Vicent, Phys. Rev. B 71, 24519 (2005).

75. B. Y. Zhu, F. Marchesoni, V. V. Moshchalkov, Franco Nori, Physica C 404, 260 (2004).

76. J. Van de Vondel, C. C. de Souza Silva, B. Y. Zhu, M. Morelle, and, V. V. Moshchalkov, Phys. Rev. Lett. 94, 57003 (2005).

77. Clecio C. de Souza Silva, J. Van de Vondel, B. Y. Zhu, M. Morelle, and V. V. Moshchalkov, Phys. Rev. B 73, 014507 (2006).

78. T. C. Wu, Lance Horng, J. C. Wu, C. W. Hsiao, Jan Koláček and T. J. Yang, J. Appl. Phys. 99, 08M515 (2006).

79. T. C. Wu, Lance Horng, J. C. Wu, C. W. Hsiao, Jan Koláček and T. J. Yang, J. Appl. Phys. 99, 08M515 (2006).

80. T. C. Wu, Lance Horng, J. C. Wu, C. W. Hsiao, Jan Koláček and T. J. Yang, J. Appl. Phys. 99, 08M515 (2006).

81. P. Hanggi, F. Marchesoni, and F. Nori, Annalen der Physik 14, 51 (2005).

82. S. Save'ev and F. Nori, Chaos 15, 026112 (2005).